DEVELOPMENT OF A REPRESENTATIVE VOLUME ELEMENT OF LITHIUM-ION BATTERIES FOR THERMO-MECHANICAL INTEGRITY

By
RICHARD LEE HILL, SR

B.S. Mechanical Engineering and Mathematical Sciences
United States Naval Academy, 2001

Submitted to the
DEPARTMENT OF MECHANICAL ENGINEERING

In Partial Fulfillment of the Degrees of

NAVAL ENGINEER
and
MASTER OF SCIENCE IN MECHANICAL ENGINEERING

at the
MASSACHUSETTS INSTITUTE OF TECHNOLOGY
June, 2011

Signature of Author: _____
Department of Mechanical Engineering
May 6, 2011

Certified By: _____
Tomasz Wierzbicki
Professor of Applied Mechanics
Thesis Supervisor

Accepted By: _____
David E. Hardt
Ralph E. and Eloise F. Cross Professor of Mechanical Engineering
Chair, Department Committee on Graduate Students

DEVELOPMENT OF A REPRESENTATIVE VOLUME ELEMENT OF LITHIUM-ION BATTERIES FOR THERMO-MECHANICAL INTEGRITY

By

RICHARD L. HILL, SR

Submitted to the Department of Mechanical Engineering on April 4, 2011 in Partial Fulfillment of the Requirements for the Degrees of Naval Engineer and Master of Science in Mechanical Engineering

ABSTRACT

The importance of Lithium-ion batteries continues to grow with the introduction of more electronic devices, electric cars, and energy storage. Yet the optimization approach taken by the manufacturers and system designers is one of test and build, an approach that nearly every other industry has long abandoned. A computational model is required to reduce the expensive build-test cycle and allow safer, cheaper batteries to be built. The path to building this computational model will involve many different processes and one of those processes dictates the homogenizing of the interior of the battery casing by treating the interior as a homogenized Representative Volume Element. This study explains this process and outlines a procedure for the development of this particular model for both cylindrical and prismatic / pouch cells.

Over twenty different mechanical tests were performed on fully-discharged cylindrical and pouched / prismatic lithium-ion batteries, in casings and without casings under multiple loading conditions. These included lateral indentation by a rod, axial compression, through-thickness compression, in-plane unconfined compression, in-plane confined compression, hemispherical punch indentation and three-point bending. Extensive testing on the battery cell and jelly roll of 18650 lithium ion cylindrical cell, combined with the use of analytical solutions to estimate material properties of the cell, yielded the development of a finite element model. It was found that the suitably calibrated model of high density compressible foam provided a very good prediction of the crash behavior of cylindrical battery cell subjected to high intensity lateral and axial loads.

For the prismatic / pouch cell, the measured load-displacement data allowed calculation of the individual compression stress-strain curves for the separator, the active anode and cathode materials. The average stress-volumetric strain relation was derived from averaging the properties of individual layers as well as from direct measurement on the bare cell. This information was then used as an input to the FE model of the cell. The model was composed of shell elements representing the Al and Cu foil and solid elements for the active material with a binder lumped together with the separator. Very good correlation was obtained between LS-Dyna numerical simulation and test results for the through-thickness compression, punch indentation and confined compression. Closed form solutions were also derived for the latter three problems which helped explain the underlying physics and identified important groups of parameters. It was also demonstrated that a thin Mylar pouch enclosure provided considerable reinforcement and in some cases changed the deformation and failure mechanism.

This paper reports on the results generated for the Li-ion Battery Consortium at MIT.

Thesis Supervisor: Tomasz Wierzbicki
Title: Professor of Structural Mechanics

Table of Contents

1. Introduction and Overview of Lithium-Ion Battery Literature 7
2. Specific Requirements for Naval Batteries 14
3. Identifying Issues with Battery Design / Safety 17
4. Mechanical Characterization of the Representative Volume Element (RVE) 18
5. Description of the Testing Program on Typical Cylindrical Batteries 22
5.1 Determination of Shell Casing Properties 22
5.2 Lateral Indentation of the Cell (with Endcaps) by a Rigid Rod 24
5.3 Compression of the Cell (no Endcaps) between Two Plates 25
5.4 Axial Crush of the Cell 26
6. Description of the Testing Program on Prismatic / Pouch Batteries 28
6.1 Description of Experiments and Details of Results 28
6.2 Compression of the Pouched Cell between Two Plates 32
6.3 Lateral Indentation of the Cell by a Hemispherical Punch 34
6.4 Unconfined Axial Crush of the Cell in the Width and Length Direction 35
6.5 Confined Compression Test of the Cell in the Width Direction 38
6.6 Three Point Bending Test of a Medium-Sized Cell 40
7. Derivation of Closed Form Solutions for Cylindrical and Prismatic / Pouch Batteries 43
7.1 Analytical Solution of Lateral Crush by Rigid Cylinder 43
7.2 Analytical Solution for the Crush Behavior of an Empty Shell 43
7.3 Analytical Solution for the Complete Cell (Outer Shell + Jelly Roll) 45
7.4 Analytical Comparison of Prismatic / Pouch Cell in the Thickness Direction 48
7.5 Punch Indentation of a Prismatic / Pouch Cell 50
7.6 Confined Compression of a Prismatic / Pouch Cell 52
7.7 Three-point Bending of a Prismatic / Pouch Cell 53
8. Numerical Simulation of Axial and Lateral Loads on Batteries 55
8.1 Finite Element Modeling of Cylindrical Cells 55
8.2 Validation of the Cylindrical Model 55
8.3 Lateral Compression of the Prismatic / Pouch Cell 58
8.4 Punch Indentation Test of the Prismatic / Pouch Cell 58
8.5 Confined Compression Test of the Prismatic / Pouch Cell 61
9. Application to the Crush Loading of Battery Modules with a Metal Housing 63
10. Conclusions and Recommendations 65
References 67

Acknowledgements

The author thanks the following individuals for their assistance in completing this thesis:

Professor Tomasz Wierzbicki for his direction and guidance on this project. His leadership was the key into turning a brief idea into a successful Lithium-Ion Consortium at MIT.

Dr. Elham Sahraei for her collaboration in writing the three academic papers from which my thesis derives. Her Finite Element Analysis modeling formed the backbone of our work.

Meng Luo for all of his assistance in the Impact and Crashworthiness Lab.

CAPT Mark Welsh for his leadership of the 2N program during our three years at MIT.

List of Figures

Figure 1 Photograph of an 18650 Lithium-ion cell cross-sectioned longitudinally 7
Figure 2 SEM image showing layer of positive and negative electrodes in an 18650 lithium-ion cell 8
Figure 3 Schematics of the four most common form factors for lithium-ion cells 10
Figure 4 Photograph of a cross section of the 18650 Lithium ion cylindrical wound cell 11
Figure 5 Small and Medium Lithium-Polymer Pouch Batteries 12
Figure 6 Multi-scale model of the battery pack spanning five orders of magnitude 19
Figure 7 The concept of Representative Volume Element 21
Figure 8 Endcaps removed, an empty 18650 shell casing, and a fractured dogbone specimen 23
Figure 9 True stress-strain curve from 18650 shell casing 24
Figure 10 Photograph of crushed cell by rigid rod and the measured load-displacement curve 25
Figure 11 Sequence of crushing during the lateral crush test 26
Figure 12 Measured load-displacement curve for three apparently identical tests 26
Figure 13 Sequence of crushing during the axial crush test 27
Figure 14 Measured load-displacement of three axial crushes 27
Figure 15 Pouch Cell with Mylar Cover Removed 28
Figure 16 Bare Pouch Cell Unrolled 30
Figure 17 Cross-section View of a Small Lithium-Polymer Cell 31
Figure 18 Measured Load-Displacement of Lateral Compression of a Bare and Pouch Cell 32
Figure 19 Experimental Stress-Volumetric Strain Curve for Bare and Pouched Cells 33
Figure 20 Engineering Stress Strain for Load-Displacement Curve of Cathode, Separator, and Anode 34
Figure 21 Load-Displacement Curve for Hemispherical Punch Indentation with Photos of Cell 35
Figure 22 Fixture Plates for Length and Width Compression of Cells 36
Figure 23 Load-displacement Response of Bare and Pouched Cells Compressed in Width Direction 36
Figure 24 Load-displacement Response of Bare and Pouched Cells Compressed in Length Direction 37
Figure 25 Photographs of Column Buckling in the Length Direction 38
Figure 26 Fixture with Battery for Confined Compression Test in the Width Direction 38
Figure 27 Axially Compressed Lithium-Ion Battery and High Density Aluminum Honey Comb 39
Figure 28 Stress Strain Curve for Confined vs Unconfined Compression in the Width Direction 40
Figure 29 Setup and Deformation Sequence of a Three-point Bending of a Battery with Pouch 41
Figure 30 Setup and Deformation Sequence of a Three-point Bending of a Bare Battery without Pouch. 41
Figure 31 Measured Load-displacement Curves of Pouch and Bare Cells Subject to 3-pt Bending 42
Figure 32 Comparison of FE simulation and closed form soln for an empty shell loaded by a rigid rod .. 44
Figure 33 Finite Element vs Analytical Solution for Lateral Compression of an Empty Shell 45
Figure 34 Assumed geometrical model of the indentation process 47
Figure 35 Yield stress versus volumetric strain of the jelly roll 48
Figure 36 Analytical vs Experimental Load-Displacement Curve for Punch Indentation of Bare Battery 52
Figure 37 Graphs Showing the Interfacial Slip in Beam with Monotonic and Reverse Curvature 54
Figure 38 The unreformed FE model of 18650 battery cell 55
Figure 39 Rigid rod indentation test versus simulation 56
Figure 40 Lateral compression between two plates 57
Figure 41 Energy absorption versus the crush distance in an axially loaded cell 57
Figure 42 FE Model of Cell and Comparison of Load Displacement Curve of Simulation to the Test 58

Figure 43 Deformation and Load-Displacement History of the Cell for Punch Indentation Simulation.... 60
Figure 44 Comparison of Hemispherical Punch Test with the Simulation.... 60
Figure 45 Confined Compression of the Cell in Width Direction with Multiple Buckles.... 62
Figure 46 Load Displacement Curve from Confined Compression Test Compared with the Simulation.. 62
Figure 47 Stress-Strain of the Cylindrical vs Rectilinear Battery Compressed in Thickness Direction..... 63
Figure 48 Prototype of Plane-Strain Compression of Pouched Batteries with Adjustable Confinement ... 64
Figure 49 Toyota Prius Hymotion battery pack and battery module 66

1. Introduction and Overview of Lithium-Ion Battery Literature

Today's Lithium-ion batteries are building blocks of very complex systems. Whether the final system is a laptop or an electric vehicle or a United States Naval ship, the desired battery packs are assembled from a system of modules, each of which typically contains a protective, tight sheet metal casing around them. Each module can be further broken down into an array of individual cells whose composition differs in the electrodes and separator from one manufacturer to another. A computed axial tomography (CT) scan through the symmetry plane of the cylindrical cell is shown in Figure 1 below:

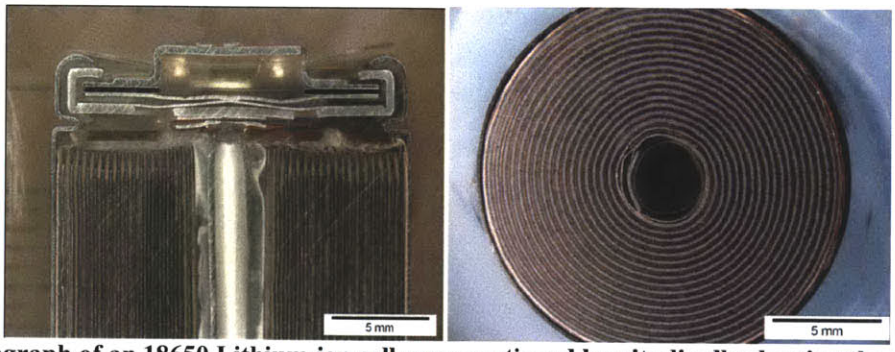

Figure 1 Photograph of an 18650 Lithium-ion cell cross-sectioned longitudinally showing the crimp and seal assembly.

There are three interrelated aspects of battery design: electrochemistry, thermal management, and mechanical integrity. The electromechanical process begins at the level of the electrode/separator assembly and most of the advances and closely-guarded secrets of the energy storage capacity are in the composition of the active electrode material with binder. Independent of exact chemistry, all Lithium-ion batteries are built in the same way: as a layered structure consisting of a negative electrode (commonly referred to as the anode), a positive electrode (commonly referred to as a cathode), a polyolefin separator between the active material of binder and electrolyte, and current collectors for both electrodes. While thicker coatings enable higher energy storage, thinner coatings enable higher power capability. A SEM image of the electrode/separator assembly is shown below in Figure 2.

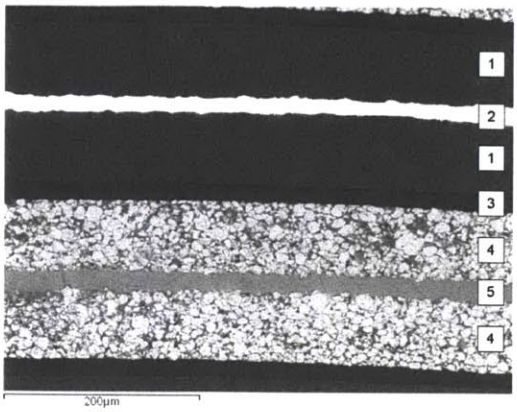

Figure 2 Scanning electron microscope image (back-scattered election contrast) showing one layer of the positive and negative electrodes in an 18650 lithium-ion cell: 1. Negative electrode coating (graphite powder), 2. Negative electrode current collector (copper foil), 3. Separator (polyethylene/polypropylene film), 4. Positive electrode coating (LiCoO2 powder), 5. Positive electrode current collector (aluminum foil) (Courtesy of Q. Horn)

While electrical and thermal integrity are equally vital, the design elements they represent change quickly as the battery chemistries evolve. **Until battery safety is optimized at the chemistry level, safe handling will continue to rely on mechanical enclosures (shell casing) as well as the protective module and pack enclosures.** As most of the strength in a battery pack or module comes from the individual cells, it becomes the most critical component in the process of the advancing Lithium-ion battery safety. This mechanical enclosure calls for the development of a computational model of an individual cell as it remains the least studied but most vital aspect of safety for electric cars. Mechanical integrity is indispensible for electrical integrity and guards against electric short circuit. Full scale 50 mph rear impact tests of an HEV performed by Lim et al (2008) proved that the peak acceleration of the battery pack reached 125g's (1). Such a pulse of a sustained duration of 25-50 ms could cause severe damage to the outer shell and electrical connections, dislodging individual cells from their resting points and further damaging the internal contacts of individual cells. Ultimately this could result in internal electrical connections being broken inside one or more battery cell resulting in a short circuit. The subsequent "thermal runaway" would then produce exceedingly high temperatures, smoke, fire, and potential explosions. The resulting high pressure inside an affected cell could result in end caps being blown off carrying this damage sequence to the neighboring cells and further spreading the catastrophic damage. While the solution to this problem continues to be pursued at the level of electrochemistry research, the protective metal casing of individual cells as well as the battery pack containment vessel remains the vital safety barrier needed to provide the requisite mechanical integrity. Several authors reported on the very severe abuse of a battery cell in the form of local intrusion by a nail, for example Otsuki et al (2006), Nguyen and Taylor (2004), Ashtiani (2009) (2; 3; 4). In most cases, the short circuit resulted in a violent event of sparks, smoke, and explosions.

General information on trends and developments in the battery industry can be found in the proceedings of the International AABC and EVS conference series. Although there is widespread agreement that crash safety of the battery pack is an important issue, very few concrete results have made their way to the open literature. This situation becomes more evident when studying recent papers published in the Journal of Power Sources. Most of the articles report on advances on electrochemistry and it is difficult to find a paper on mechanical properties of the jelly roll (interior of the battery cell) leading to the build-up of a computational model. While that there have been several efforts to model mechanical behavior of batteries in the elastic range (Zhang et al 2007 and 2008, Chen et al 2006, Golmon et al 2009) (5; 6; 7), elastic analysis itself provides no clues about failure of internal and external components of battery cells, including failure of the separator leading to short circuit. It is hoped that the present research will contribute to the quest to place battery structural/electrical integrity on a firm theoretical and computational ground. A general procedure will be outlined on the development of a constitutive and computational model for both a cylindrical cell and a prismatic cell. It will be shown that an average homogenized property of a battery cell combined with a constitutive model of high density foam can be determined through a combination of physical testing and closed form solutions.

Anatomy of a Lithium Ion Cell

In its simplest form a battery is an electrochemical energy storage device that converts stored chemical energy into electrical energy. Independent of chemistry, all batteries consist of a negative electrode, a positive electrode, a separator, electrolyte, and current collectors for both electrodes. In a lithium-ion battery, these components are:

- Negative electrode (anode) active particles (graphite) with binder and electrolyte
- Positive electrode (cathode) active material (transition metal oxide or phosphate ($LiCoO_2$ most common)) with binder and electrolyte
- Polyolefin separator: nano-porous polyethylene/polypropylene film
- Negative electrode current collector: copper foil
- Positive electrode current collector: aluminum foil
- Electrolyte: $LiPF_6$ dissolved in a solution of organic carbonates

When a Lithium-ion cell is charged and discharged, Lithium-ions (Li^+) shuttle between the negative and positive electrodes as it diffuses into and out of the crystal lattice of the active materials. One of the more common chemistries is offered below:

$$cathode\ reaction:\ \ CoO_2 + Li^+ + e^- \rightarrow LiCoO_2$$

$$anode\ reaction:\quad LiC_6 \rightarrow Li^+ + 6C + e^-$$

To reduce the diffusion distances of the ions, the active material format most commonly utilized is powder. This powdered active material is coated onto the foil current collectors with the coating thickness optimized for the battery's energy and power capability. Thicker coatings enable higher energy storage while thinner coatings enable higher power capability.

To make a Lithium-ion cell, alternating layers of positive electrodes, negative electrodes and separator are stacked or wound onto an electrode assembly. The electrode assembly is then placed into a container that is sealed to prevent oxygen and moisture ingress as well as electrolyte egress. The shape of the container and its material define the "form factor" of the cell. The four most common form factors for lithium-ion cells are cylindrical, prismatic, coin and pouch, which are shown schematically in Figure 3 below.

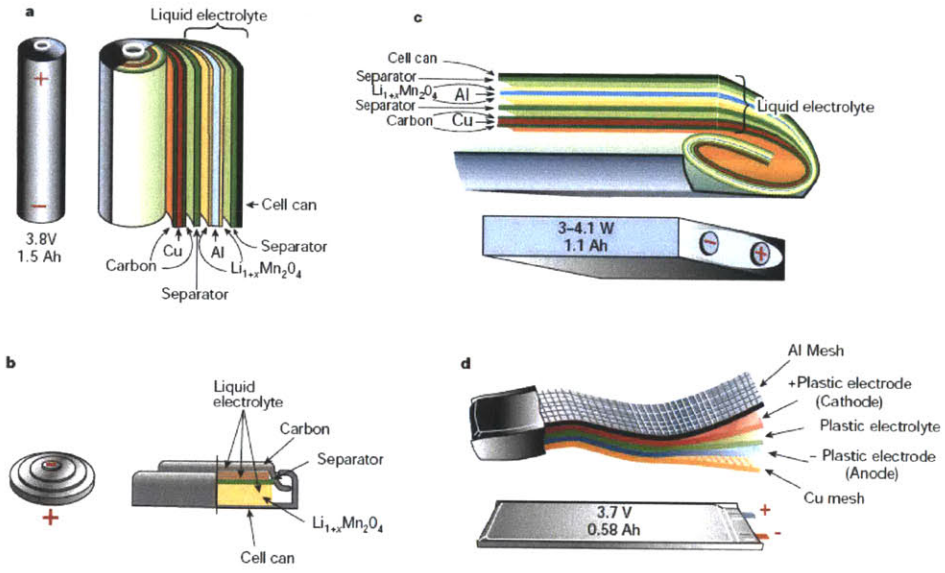

Figure 3 Schematics of the four most common form factors for lithium-ion cells: a. cylindrical, b. coin, c. pouch (also referred to as "polymer"), and d. prismatic (wound prismatic shown) (Tarascon and Armand, 2001) (8) .

The most commonly manufactured Lithium-ion form factor is the cylindrical 18650 cell. The number "18650" refers to the cell size, which is 18 mm in diameter and 65 mm in length. The 18650 has a spiral-wound electrode assembly (commonly referred to as a "jelly-roll") that is encased in a metal can (usually steel), and closed by crimping the steel can around the seal assembly. Photographs of a cross-sectioned, commercially available 18650 cell (with crimp/seal assembly) were shown earlier in Figure 1. The microstructure of the wound electrode assembly within a Lithium-ion 18650 cell can be examined by cross-sectioning the Lithium-ion cell in an axial orientation. The high magnification, scanning electron

microscope image of this cross-section cell was shown earlier in Figure 2, where the electrode coatings, current collectors and separator are clearly visible. The first order constitutive model of the cylindrical cell is described later in this paper. A tight winding process combined with considerable constraints in the radial and axial direction offered by the shell casing resulted in a relatively isotropic response of the jelly roll. It was then possible to model the battery by introducing a concept of the Representative Volume Element, RVE, shown in Figure 4a and 4b.

In addition to the model of the cylindrical cell, an attempt was also made to develop a computational model of the prismatic and/or pouch batteries. A common feature of the prismatic / pouch batteries is that the electrode/separator assembly is stacked instead of wound, Figure 4b below. Equally important is that the typical length dimension is much larger than the thickness. For example, one commercially available pouch battery is 5 mm thick, 30 mm wide and about 60 mm length. The actual dimensions are not important; it is the length-to-thickness ratio that matters. The prismatic batteries can be considered as multi-layered anisotropic thick plates. The pouch batteries are sealed inside a flexible, thin plastic or aluminum cover while the prismatic batteries are housed inside a more-rigid plastic or metal container. Because of large unsupported area, the cladding offers considerable resistance in some loading directions and very little in others. This type of "form factor" is prone to delamination and buckling. The buckling strength of the cell compressed in the width and length direction is relatively low due to the lack of shear and/or tension forces transmitted between individual layers. The prismatic/pouch batteries do not resist compressive loads as a monolithic plate but instead as a loose collection of thin plates with some random interactions. There is a very interesting duality in the behavior of such structures. They are highly anisotropic at the micro scale. They are isotropic at the size of the representative volume element. The whole cell is then structurally anisotropic.

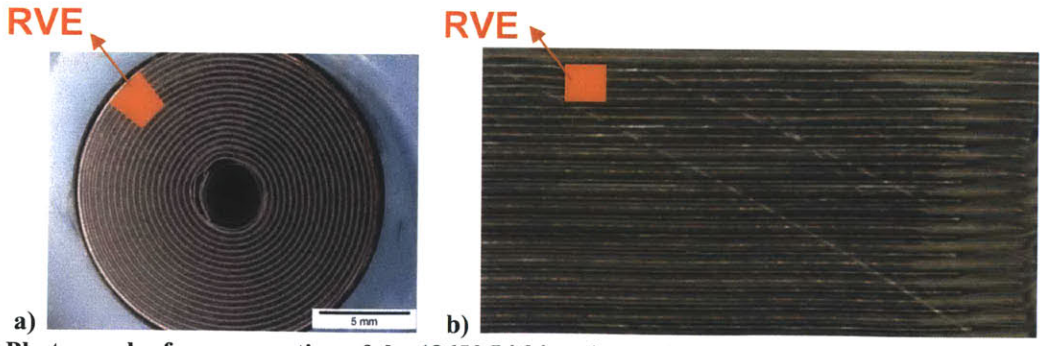

a) b)

Figure 4 Photograph of a cross section of the 18650 Lithium ion cylindrical wound cell (a) and typical stacked profile (b) of a prismatic/pouch cell

Unlike prismatic or cylindrical cells which contain a sheet-metal casing, pouch cells utilize a thin lightweight covering which allows a more flexible cell. For the purposes of mechanical modeling, the prismatic and pouch batteries will be represented identically in this report. For this study, the 18650 cell was chosen to represent the cylindrical category and two types of pouch cells were chosen to represent prismatic/pouch:

Table 1 Dimensions of Lithium Polymer Pouch Cell Interiors Chosen for Testing

	Thickness (mm)	Width (mm)	Height (mm)	Mylar Thickness (mm)
Small	5	30	50	0.140
Medium	8	30	130	0.110

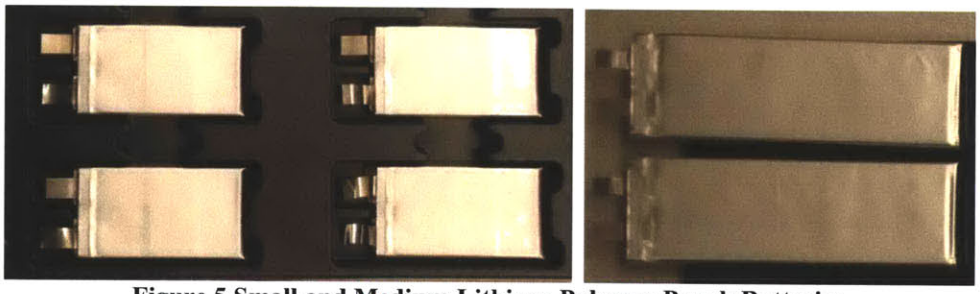

Figure 5 Small and Medium Lithium-Polymer Pouch Batteries

Two new parameters are controlling the deformation process: the length scale and amount of lateral through-thickness constraints. In this paper an insight into mechanical performance is gained by physical testing (section 3), model development (section 4) and numerical simulation (section 5). The presented mechanical model of cylindrical cells and prismatic batteries are indispensible tools for the weight-efficient and safe design of batteries. Such models are currently absent in the open literature.

The exact mechanical properties of lithium-ion batteries subjected to various types of loading depend on the "form factor". This form factor is determined by the particular arrangement of the electrode/separator assembly which may be wound, forming a cylindrical shape, or stacked, creating a prismatic shape. All batteries, both cylindrical and prismatic/pouch, possess the same fundamental components of coated anodes and cathodes sandwiched by layers of separator. The anode typically has a coating of graphite in a binder while the cathode is coated by metal oxide with a binder. As the separator is very thin (0.01 mm) and weak compared to the strengths of aluminum/copper foil of the electrodes, it contributes little to the overall strength of the individual cells. This present paper reports the test program and model development of cylindrical and prismatic/pouch batteries which are created by rolling or stacking individual layers of electrode/separator.

Typical laboratory tests require cutting relatively small specimens from larger blocks in order to fit standard fixtures and to avoid exceeding the limits of testing equipment. Instead of cutting specimens into rectilinear shapes, which by itself poses a formidable problem, the pouch batteries already possess the ideal dimensions for laboratory tests. Unlike prismatic or cylindrical cells which contain a sheet-metal casing, pouch cells utilize a thin covering (typically Mylar) which allows a more flexible cell due to the less rigid, lightweight shell.

2. Specific Requirements for Naval Batteries

The United States Navy uses many different types of batteries, from alkaline disposables to the long-preferred reliable, rechargeable Pb-acid which is now transitioning to Absorbed Glass Matt, to NiCd to NiMH and now Li-ion. Lithium-ion's very flat discharge profile offers the best battery from a volumetric and gravimetric power density standpoint. As a disadvantage, Lithium-ion is potentially more dangerous than other chemistries due to flammable electrolyte, fuel, and lithium metal formations.

Lithium-ion battery chemistries continue to advance rapidly. The power densities offered greatly expand the current design scope of power storage, offering more kW-hours of energy at a smaller weight and volume penalty as compared to traditional lead acid batteries. Additionally, as shown by the table below, these newer chemistries such as $LiFePO_4$ offer cycle lives that may be ten times more than that of the Sealed Lead Acid (SLA).

Table 2: Comparison Between Different Battery Types (9)

Chemistry	Voltage	Energy Density	Working Temp	Cycle Life	Safety	Environ-mental	Cost based on cycle life x wh of SLA
Sealed lead acid	2.0V	> 35 wh/kg	-20 to 40 deg C	>200	Safe	Not good	1
Nickel Cadmium	1.2V	> 40 wh/kg	-20 to 50 deg C	>1000	Safe	Bad	0.7
Nickel Metal Hydride	1.2V	> 80 wh/kg	-20 to 50 deg C	> 500	Safe	Good	1.2 - 1.4
LiMnxNiyCozO2	3.7V	> 160 wh/kg	-20 to 40 deg C	> 500	Unsafe without PCB or PCM, better than LiCo	OK	1.5 - 2.0
LiCoO2	3.7V	> 200 wh/kg	-20 to 60 deg C	> 500	Unsafe without PCB or PCM	OK	1.5 - 2.0
LiFePO4	3.2V	> 120 wh/kg	0 to 60 deg C	> 2000	Safe	Good	0.15 - 0.25

Lead also continues to grow as an environmental concern. By removing the lead in favor of the newer Lithium-ion chemistry a safer, more environmentally-friendly substitute is realized, further reducing disposal and hazardous-material handling costs. These significant environmental costs are difficult to estimate in the design stage and good designs will strive to minimize their use before construction.

LiCoO2 (lithium polymer) represents a sizeable portion of the pressure-tolerant battery market. These batteries are incredibly power-dense and are very safe by the use of an installed Protection Circuit Module (PCM) or Protection Circuit Board (PCB) which prevents the batteries over-charging or over-discharging. However, these batteries come at a significant price increase compared to SLA.

LiFePO4 represents a relatively new battery discovered in 1996 that has the preferred characteristics of low cost, non-toxic, high energy capacity, and good thermal and electrochemical performance. The low electrical conductivity experience initially has been recently overcome (10) and this new blend has rapidly entered mass-production by numerous major corporations such as DeWalt, GM, Daimler, Cessna, and BAE Systems .

Recent problems with Lithium-ion have further underscored the need for a cautious testing and acceptance program. One example is the Advanced Seal Delivery System (ASDS). The ASDS was a long-range submersible capability to deliver special operations forces for clandestine missions. ASDS provides improved range, speed and payload, and habitability for the crew and a SEAL squad. ASDS will be carried to its designated operational area by a host ship, a specially configured SSN-688 Class submarine. ASDS will also be air transportable by either C-5 or C-17 aircraft. A total of six ASDS will be built for USSOCOM. This manned dry interior battery-powered submersible is managed by the NAVSEA PMS 395 Deep Submergence Directorate and developed by Northrop-Grumman Ocean Systems. A component of Northrop Grumman's Baltimore, Md.-based Electronic Sensors and Systems Division, Oceanic Systems employs approximately 700 people engaged in designing, producing, testing and supporting some of the world's most sophisticated undersea systems. A detailed design and manufacturing development contract was awarded in FY 1994. The program suffered several setbacks even before the fire that ravaged the ASDS vehicle. As is happening to most U.S. Navy ship programs, the ASDS "vehicle" was behind schedule and far over cost projections. The vehicle was completed in 2001 by Northrop Grumman's Ocean Systems in Annapolis, Maryland, and was "conditionally" accepted by the Navy. In 2003 it was assigned to SEAL Delivery Vehicle Team 1 at Pearl Harbor. The craft suffered major problems with its propulsor, electrical system, and batteries. (Its original zinc batteries were replaced with lithium-ion batteries.) Because of these and other problems, plus cost increases, in 2006 the U.S. Special Operations Command -- sponsor of the program -- and the Navy cancelled the procurement of the five planned additional vehicles. The lithium-ion batteries were being charged, with the craft on shore when the fire erupted on 9 November 2008 and burned for six hours. According to Christopher P. Cavas, writing in *Navy Times* newspaper, "firefighters sealed the ASDS to put out the fire and continued to hose it down for several hours to cool hot spots. The mini-sub remained sealed for more than two weeks before the hatch was opened." (11) The Navy estimates repairs to the 60-ton craft would cost $237

million, or $180 million more than the craft's operating budget, and take nearly three years to complete. "Competing funding priorities ... prevent the command from repairing the ASDS," said U.S. Special Operations Command (USSOCOM) in a statement released July 24. There are no plans to fix the ASDS in the future, said USSOCOM spokesman Lt. Cmdr. Fred Kuebler. (11) While the problems could have been caused by a simple malfunction, the range of damage is overwhelming.

3. Identifying Issues with Battery Design / Safety

The US Navy is concerned with the safety of any type of battery. One concern of any battery is battery venting. In normal venting the battery allows a controlled release of a cell's electrolyte through the designed venting mechanism. Cell defects or abuse may result in venting that may be too high for the installed vent, resulting in an unplanned release of internal pressure by ejecting some or all of the internal components into the environment which may release:

a. flammable organic material
b. $LiPF_6$ which reacts with water to produce hydrofluoric acid (HF)
c. Carbon either as carbon or water reactive lithiated graphites
d. LiNiCoO2 or lithiated oxides and heavy/transition metals
e. Metal foils and fragments (copper or aluminum)
f. Methane, hydrogen, carbon monoxide (electrolytic decomposition products)

Ventings may also be accompanied by smoke, sparks, and or flames. Typical mistreatment of batteries includes:

a. physical abuse such as crushing, puncturing, or burning
b. overcharging due to electronics failure
c. exposure of battery to inapprorpriate environment (high heat or water immersion of an unsealed battery)
d. short circuit or abnormally high rate of discharge
e. improper use of or incorrect batteries used in an item

As a result of these concerns, the US Navy has stringent testing procedures designed to test batteries in a full range of environments and abuse scenarios. While this is undoubtedly better than the industries' limited battery of tests, it is nonetheless a slow, methodical and costly process. What is needed is a computational model built from accepted test methods that allows rapid development and feedback. In turn, these models will allow a full understanding of the risk to personnel, equipment, and host platforms.

4. Mechanical Characterization of the Representative Volume Element (RVE)

This thesis proposes the method of building constitutive and computational models of the lithium-ion battery from the smallest constituents of a jelly roll (aluminum and copper electrode collectors, anode and cathode active material and the separator) through surrounding shell casing, assembly of individual cells into modules and all the way to the entire battery pack. Development of such a multi-scale model will require a complex system of many different types of tests, complex calibration procedures, validation and finite element implementation.

The conceptual flow chart explaining how the model will be built is shown in Figure 6 below. **The model spans five orders of magnitude in length.** The development of each higher level model draws from the analytical, numerical and experimental results obtained from the preceding level. The order in which the levels interact with one another depends on the specific application. If the objective is to study the effect of initial existing or nucleated flaws on thermo-mechanical integrity, the order of interactions will be from top down beginning with the large battery pack. The same will apply for the optimization procedure.

If, on the other hand the crash safety is of concern, then one would track down Table 1 from bottom up, starting with the smallest component of the separator. A crash event produces high deceleration (125 g), as well as possible intrusion into the battery pack. This can lead to a multitude of different failure modes of the interior of the battery pack. The outer shell could also be severely damaged and cracked, spot-welded electrical connections between the cells and the nickel current collector plates can be broken, and the individual cells could be dislodged from their resting position. Then the cells can interact and crush against each other causing further damage to the internal components of individual cells, including tearing of the separator. This would result in a short circuit, and the subsequent shut off of a battery or the "thermal runaway", leading to exceedingly high temperatures, smoke, fire, and potential explosions. The resulting high pressure inside an affected cell could also result in end caps being blown off causing possible damage to the neighboring cells and further spread the catastrophic damage.

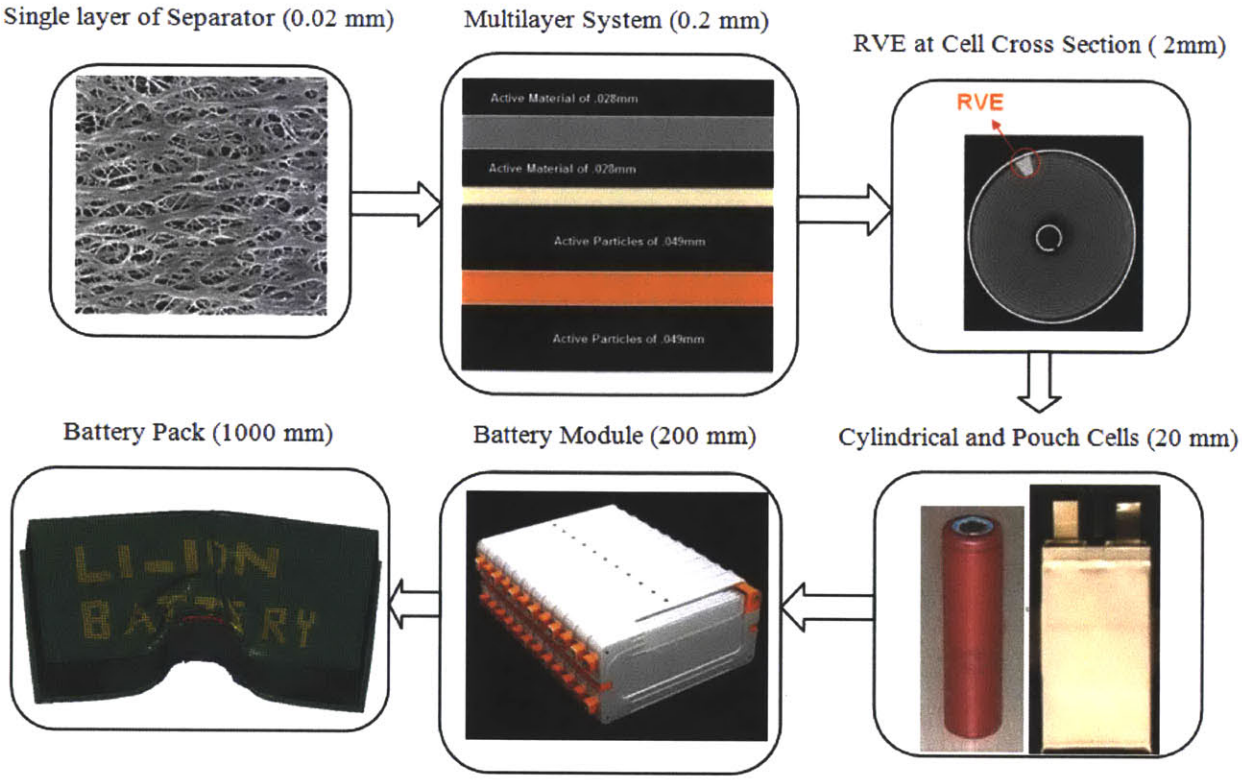

Figure 6 Multi-scale model of the battery pack spanning five orders of magnitude

This multi-disciplinary multi- scale and multi material research effort should be divided into four stand-alone projects. Each project will have its own objective, statement of work and set of deliverables. All projects will have five major ingredients:

- Theoretical framework
- Tests for model identification
- Finite element implementation
- Validation
- Applications

List of Proposed Projects

Project 1 Development of a Constitutive and Computational Model of the Electrode/Separator Assembly

Task 1.1 Modeling of individual layers and the electrode/separator assembly

Task 1.2 Testing program on 0.02-0.2 mm scale

Task 1.3 Finite element implementation and development of users' subroutines in LS-Dyna and ABAQUS

Project 2 Development of a Homogenized Model of Entire Battery Cell

Task 2.1 Representative Volume Element (RVE) and averaging procedure

Task 2.2 Testing program on cylindrical and prismatic battery cells

Task 2.3 Modeling fracture of shell casing including end caps and spot-welds

Task 2.4 Determination of Mechanical Properties of the Battery Interior (Jelly Roll)

Project 3 Industrial Applications (with active participation of industrial sponsors)

Task 3.1 Prediction of the electrical short circuit and battery thermal runaway under various loading conditions through numerical simulation.

Task 3.2 Study of failure of electrode/separator during the charging/discharging cycles.

Task 3.3 Quantification of the advantages of cylindrical vs. prismatic battery design from the point of view of thermo-mechanical integrity.

Project 4 Optimization of Individual Cells and the Battery Pack for Minimum Weight and Crash Safety

Task4.1 Optimization at the level of the electrode/separator assembly (choice of the binder, strength of interface between various layers, alloy thickness of electrodes)

Task 4.2 Optimization at the level of a battery cell (with active participation of industrial sponsors) (Choice of material and thickness of shell casing, design of end caps and safety valves, cylindrical versus rectangular configuration)

Task 4.3 Optimization at the level of the battery pack (effect of supporting trays, properties of cooling agent, magnitude of cooling gaps, choice of sheet metal, design of brackets, attaching the battery pack to the car body)

This paper details the results of task **Task 2.1** Representative Volume Element (RVE) and averaging procedure which is only one step in the complicated task of optimizing batteries for robust mechanical design.

Task 2.1 Representative Volume Element (RVE) and averaging procedure

A practical solution to FE modeling of the cell is to employ much larger homogenized elements, referred to as RVE elements. Such an element would comprise 5 to 10 windings so that the size of an element will be on the order of 2x2x3 mm, see Fig. 10a. The total number of solid elements representing a single cylindrical cell would then become about 5000. The number of RVE elements in a large prismatic cell will be 50,000, which remains manageable.

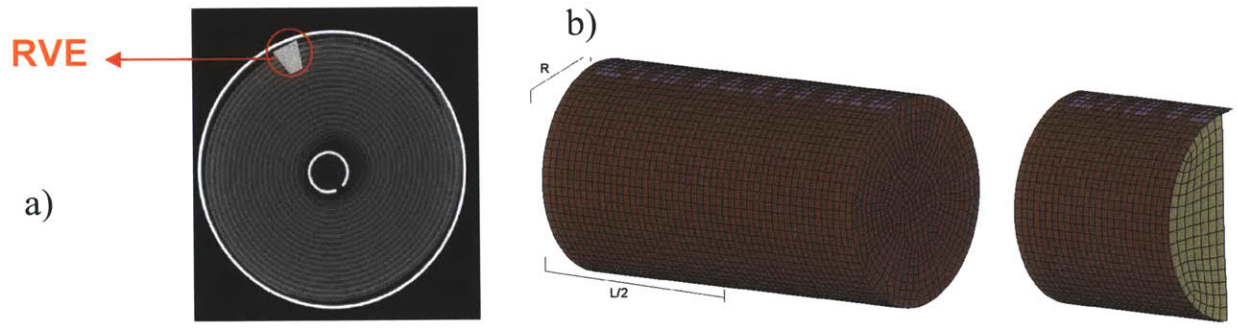

Figure 7 The concept of Representative Volume Element reduces substantially the size of the FE model (a) Full model, and a quarter model of the battery cell discretized by large RVE homogenized elements for core winding (b)

Direct Averaging Procedure Having determined mechanical properties of all constituents of the electrode assembly in Project 1, a macroscopic, homogenized model of the actual material will be developed. Following the work by Sahraei et al (2010) the stresses in the RVE will be averaged under the prescribed uniform strain or displacement at the prescribed boundaries (12). For that purpose a separate subroutine in LS Dyna and Abaqus will be developed. Then, numerical simulation of the local response of the core winding will be determined for different conditions of loading. On that basis a relationship between average stresses and strains will be obtained in a finite or incremental form. The direct averaging method will provide data for the discharged battery only.

5. Description of the Testing Program on Typical Cylindrical Batteries

Only fully discharged cells were tested in the MIT Impact and Crashworthiness Lab to minimize environmental hazards. Few special labs with atmospheric hoods are able to test charged, even very small, Lithium-ion cells. Larger cells charged to full capacity would require special testing facilities that could withstand massive thermal events. Such test facilities are operational at Naval Surface Warfare Center Crane, IN and are also under construction in Germany. The MIT test program was conducted both with and without endcaps as the uncapped batteries allowed observations to be conducted of the compressed jelly roll throughout the full range of tests. Hazardous controls consisted of testing only completely discharged cells and then tightly controlling any spilled electrolyte.

5.1 Determination of Shell Casing Properties

The plastic properties of the shell casing were not obtained from the manufacturer, but rather, determined from our own tests. The manufacturing process for battery casings consists of deep drawing of cans from rolled steel sheets. Both the rolling and drawing processes introduces some amount of anisotropic properties which, while normally pronounced in aluminum, is typically less important in steels. Therefore the material is taken as being isotropic and therefore, the tests in only one direction are sufficient. Tensile tests were performed on dogbone specimens cut from the shell casing. To create dogbone specimens, the endcaps were removed from 18650 cells. The positive terminal endcap was removed by a tubing cutter which evenly removed the endcap. The negative side, however, required the use of a cutting tool on the ninety degree edge of the endcap. After cutting away that edge, the endcap could then be removed exposing the jelly roll. Neither method damaged the jelly roll. Then the jelly rolls were gently removed and the casing was cleaned (see Figure 8 below).

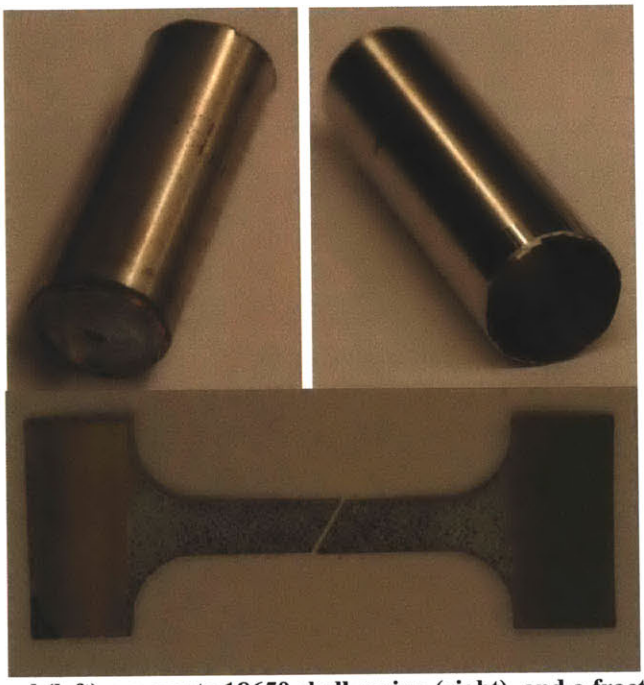

Figure 8 Endcaps removed (left), an empty 18650 shell casing (right), and a fractured dogbone specimen (bottom)

Now the empty casing was cut lengthwise and unrolled. Care was taken to unroll the empty casing which exhibited a great deal of springback. Only the essential amount of stress was applied to unroll the specimen for cutting into a dogbone shape. The final shape of the dogbone specimen was cut using a waterjet by placing the thin shell casing between two thicker plates of steel to keep it flat. Double-sided tape was also used to aid in maintaining it flat for the waterjet.

Digital Image Correlation (DIC) was used to measure local strain. Load-displacement was measured using an MTS 200 kN Universal Test Machine with a 10 kN load cell.

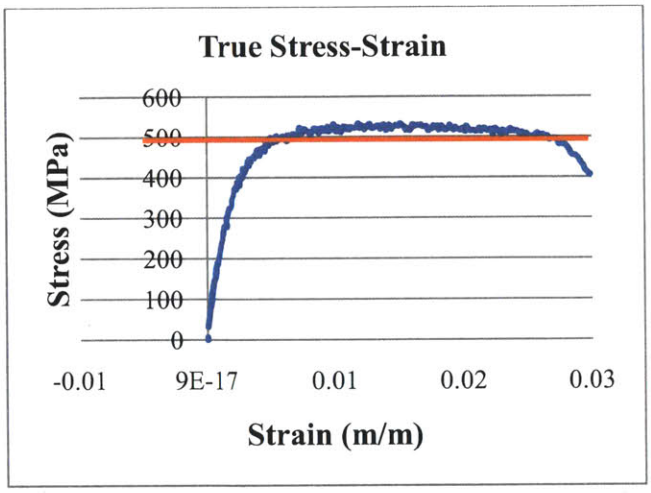

Figure 9 True stress-strain curve from 18650 shell casing

From the above true stress-strain curve (Figure 9), the average flow stress of the shell casing was estimated to be σ_o = 500MPa. This value is important in the analytical solution of the shell casing which will be discussed in the next section.

5.2 Lateral Indentation of the Cell (with Endcaps) by a Rigid Rod

One of the standard destructive tests of batteries consists of pressing the battery with a rigid lateral indenter. For the purposes of this paper the indenter was chosen as a rigid rod of diameter 12.2mm which is approximately 2/3 of the diameter of the cell. During the test the battery cell wrapped tightly around the rod and the endcaps rotated and lifted slightly from the bottom plate (see Figure 10 below).

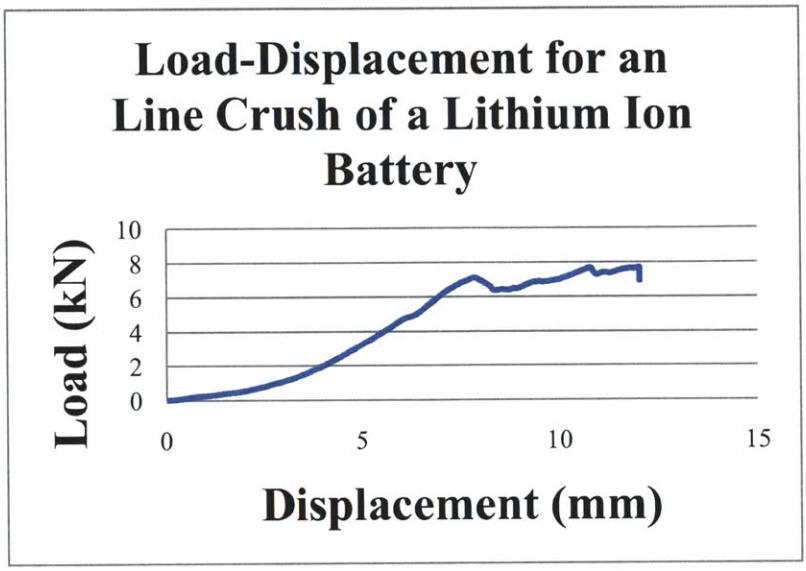

Figure 10 Photograph of crushed cell by rigid rod (above) and the measured load-displacement curve (below)

The measured load-displacement curve of the test is shown in Figure 10. One can observe two phases of the crushing process. In the first phase there is almost a parabolic increase in resistance up to about 8mm crush distance. After that some other complex phenomenon takes place and the crushing strength remains more or less flat.

5.3 Compression of the Cell (no Endcaps) between Two Plates

For the remaining two types of tests, the endcaps were removed to allow full observation of the jelly roll during crushing. Additionally, this prevented the endcaps from acting as bulkheads which would resist the crushing motion and for which no easy analytical solution exists. A photographed sequence of the deformation mode of the cross-section of the cell is shown in Figure 11 below. Individual windings which form two flat plates joined by two half-cylinders are easily distinguished. The core support initially provides support but initial compression flattens it and the later photographs missing the core support validate this. The measured load-displacement curve is shown in Figure 12 below.

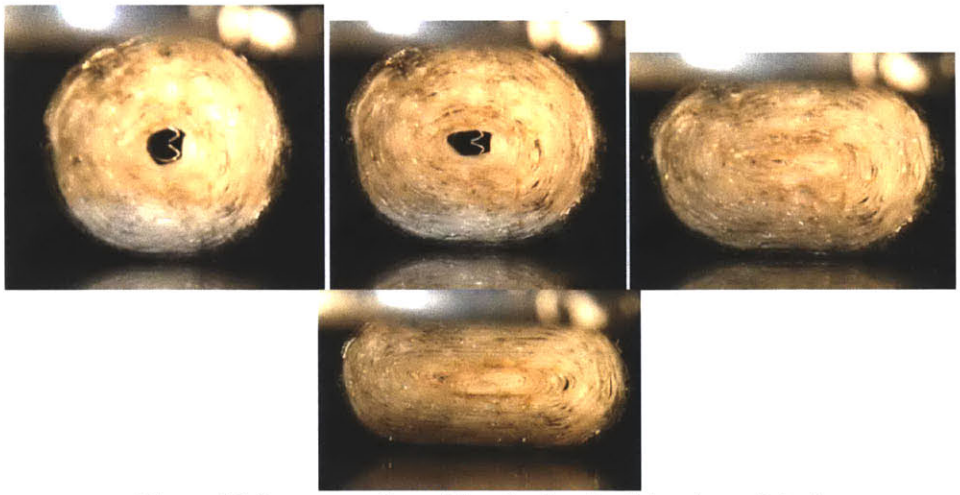

Figure 11 Sequence of crushing during the lateral crush test

Three tests were performed, establishing repeatability. A comparison of the measured load-displacement curve is shown below in Figure 12. Up to 7mm crush distance the results are nearly identical.

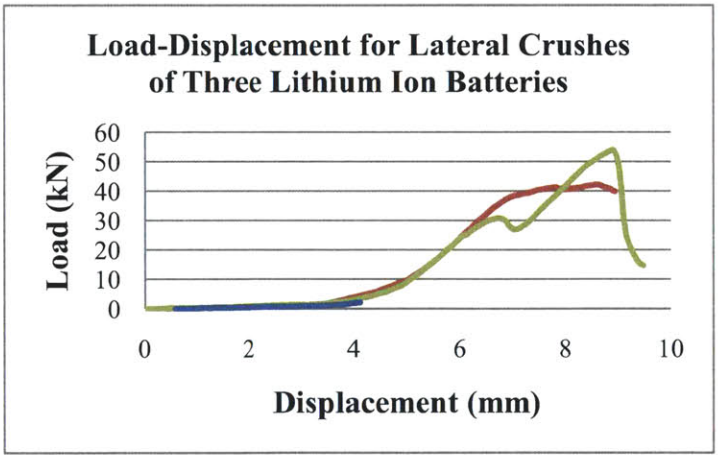

Figure 12 Measured load-displacement curve for three apparently identical tests

5.4 Axial Crush of the Cell

In the axial direction three tests were run with all endcaps removed to minimize hydraulic buildup of the electrolytic fluid which could have resulted in a rupture prematurely ending the test. The slight disparity between the tests may indicate that the batteries are still sealing against the test surface during the crush. Axial crush tests required the use of a retention device which prevented a shear type of crush mode. In this particular test the retention device was a ¾" inner diameter washer further milled to the outside

dimension of the cylindrical cell. This washer, once affixed to the fixture, prevented side-movement of the cell during compression. The sequence of the deformation mode is shown below in Figure 13. Axi-symmetric folds are shown initiating at one end of the cell. Then a phase of progressive fold formation occurs followed by the development of folding at the center of the cell. This behavior is fully consistent with the results of other investigations where cylinders filled with polyurethane and aluminum foam were subjected to axial crush (13; 14; 15; 16; 17).

Figure 13 Sequence of crushing during the axial crush test

Three tests were performed showing very good repeatability (Figure 14). This concludes the experimental portion of the cylindrical batteries. Additional graphs not used in the report are provided in the attached Appendix.

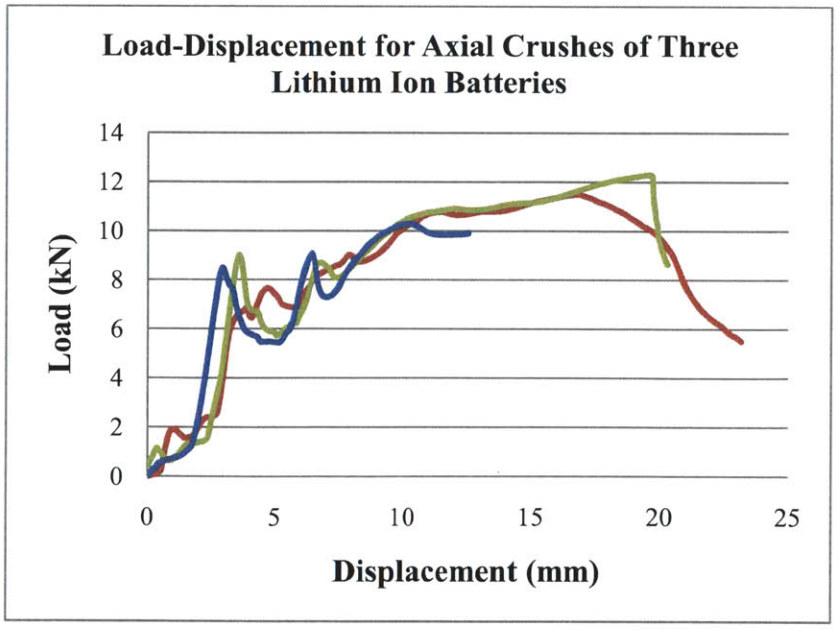

Figure 14 Measured load-displacement of three axial crushes

6. Description of the Testing Program on Prismatic / Pouch Batteries

Like the cylindrical tests, only fully discharged cells were tested in the MIT Impact and Crashworthiness Lab to minimize environmental hazards. Typical laboratory tests require cutting relatively small specimens from larger blocks in order to fit standard fixtures and to avoid exceeding the limits of testing equipment. Instead of cutting specimens into rectilinear shapes, which by itself poses a formidable problem, it was decided to work on pouch batteries which already possess the ideal dimensions for laboratory tests. Unlike prismatic or cylindrical cells which contain a sheet-metal casing, pouch cells utilize a very thin covering which allows a more flexible cell. For the present study that is aimed at developing general testing and modeling procedures, the choice of a particular manufacturer is unimportant. All batteries, both cylindrical and prismatic/pouch, possess the same fundamental components of coated anodes and cathodes sandwiched by layers of separator. The anode typically has a coating of graphite in a binder while the cathode is coated by metal oxide with a binder. The sizes of the commonly available pouch batteries which were chosen for this paper were detailed earlier in Table 1 and Figure 5.

Both small and medium batteries tested were wrapped tightly by a Mylar casing. Mylar sheets have a relatively low elastic modulus of 3-4 GPa but a tensile strength of approximately 180 MPa. This relatively strong casing contributed significantly to the strength of the entire cell. Therefore half of the tests were performed on as-received batteries in the enclosing pouch and half bare with this Mylar cover removed, as shown in Figure 15 below. While only fully discharged cells were tested in the MIT Impact and Crashworthiness Lab to minimize environmental impact, hazardous controls further consisted of tightly controlling any spilled electrolyte.

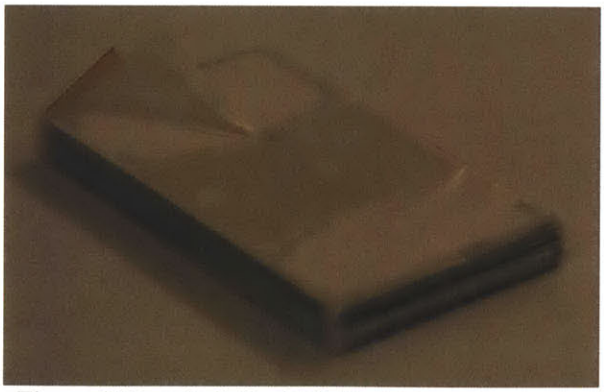

Figure 15 Pouch Cell with Mylar Cover Removed

6.1 Description of Experiments and Details of Results

Seventeen batteries were tested under compressive load in five different load applications.

1. Compression of the Pouched Cell Between Two Plates
2. Lateral Indentation of the Cell by a Hemispherical Punch
3. Unconfined Axial Crush of the Cell in the Length and Width Direction
4. Confined Compression Test of the Cell in the Width Direction
5. Three-Point Bending Test of a Medium-Sized Cell

In all cases, the output of the experiments consisted of the measured load-displacement curve and photographs of the sequenced deformation. The Digital Image Correlation (DIC) available in the lab was not utilized in this preliminary round of tests. In future experiments the DIC will be particularly valuable in determining local displacement and strains. All tests were performed on an MTS load frame with either 10 kN or 200 kN load cells depending on the loading direction. The crosshead speed was chosen to vary between 0.5 and 3 mm/min. Testing of batteries under higher strain rates is the subject of future research.

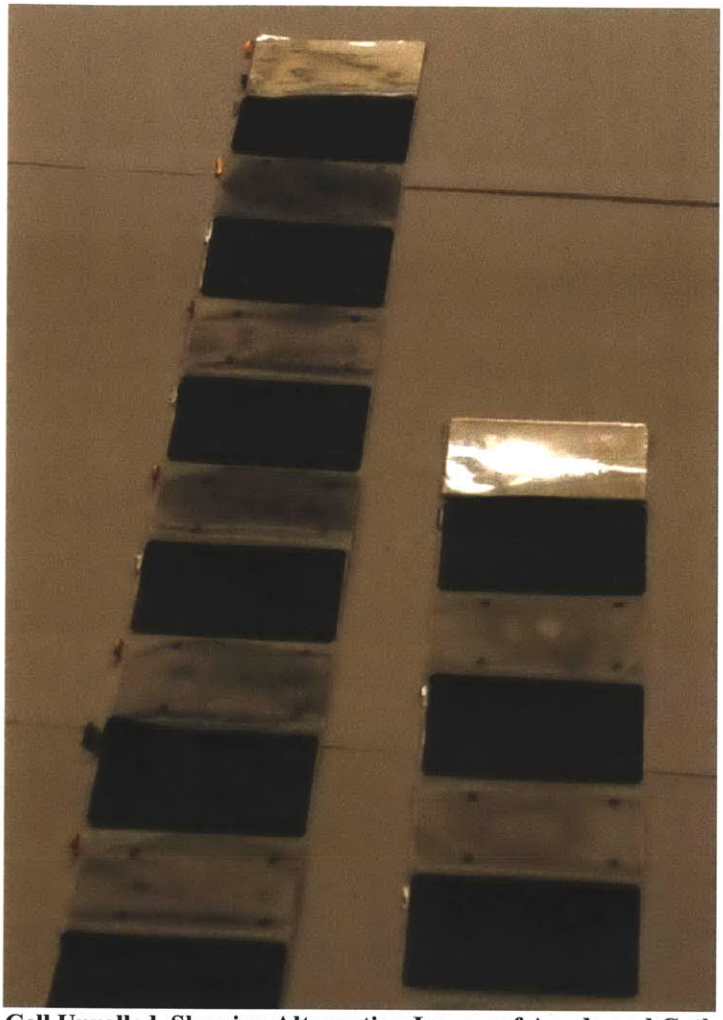

Figure 16 Bare Pouch Cell Unrolled, Showing Alternating Layers of Anode and Cathode Plates Adhered to Separator

In order to take thickness measurements of individual components, the small pouch battery was disassembled by removing the Mylar pouch, Figure 16 above. The coated anodes and cathodes were easily disconnected from the polymeric separator, similar to a stack of cards. The active particle with binder was firmly adhered to the metallic foils. Altogether, there were 20 individualized copper anode plates, 18 double-sided coated aluminum plates, and 4 single sided coated aluminum plates, all separated by over 46 cell-sized layers of continuous separator. The thickness of the individual copper and aluminum plates was measured by washing away the active coating using a solvent in a vent hood. The thickness of the coated current collectors was measured both individually and as a stack and by dividing the stack height by the number of plates. Both methods gave near identical results. All data gathered is presented below in Table 3 and further illustrated by Figure 17 below.

Table 3 Direct Measurements Obtained of Small Lithium Polymer Cell Contents

All measurements in mm	length	width	measured thickness	calculated thickness
Cu anode double-coated	50	30	0.117	0.116
Al cathode single coated	50	30	0.056	0.055
Al cathode double-coated	50	30	0.080	0.079
Separator	51.8	32	0.013	0.021
Copper foil	50	30	0.025	-
Aluminum foil	50	30	0.025	-

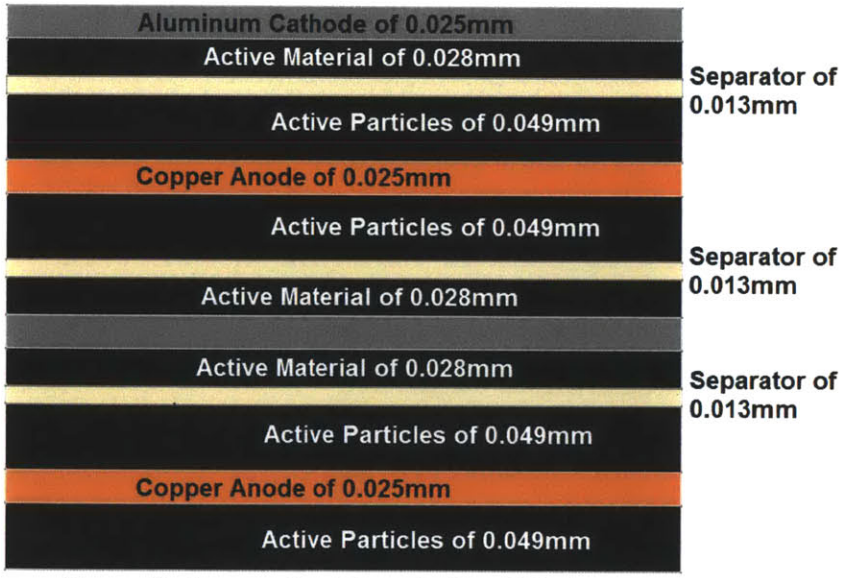

Figure 17 Cross-section View of a Small Lithium-Polymer Cell

In order to keep the battery brand anonymous, it was decided to perform all measurements directly in the lab rather than requesting the data from the manufacturer. Future experiments could benefit from the time-savings of using manufacturer-supplied data.

6.2 Compression of the Pouched Cell between Two Plates

Two batteries, one bare cell and one cell contained in the original Mylar pouch, were subjected to lateral compression of up to approximately one-half of the thickness. The recorded load displacement relationships are shown in Figure 18 below.

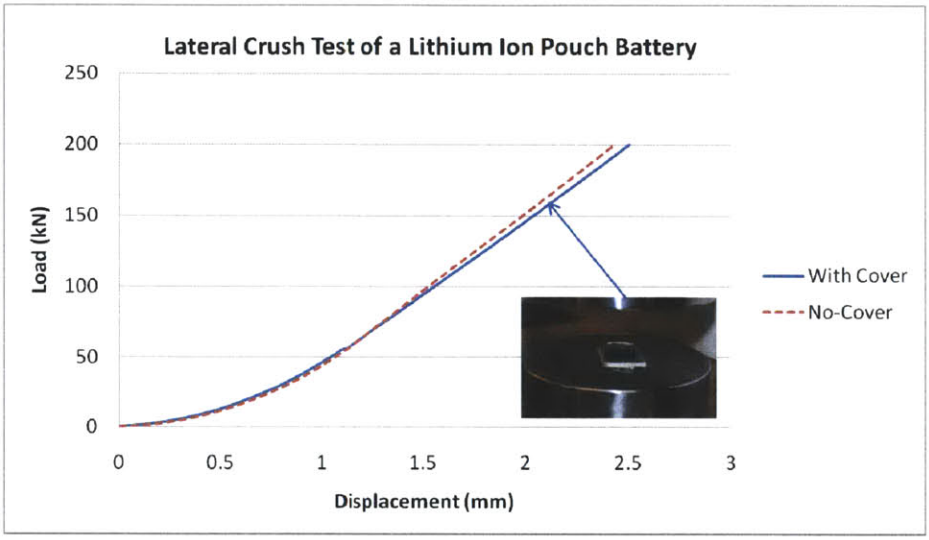

Figure 18 Measured Load-Displacement of Lateral Compression of a Bare and Pouch Cell

At this crush distance, the force level is near the load-limit of the 200 kN MTS testing machine. In both cases, the electrolyte was squeezed from the cells which allowed for a volumetric change. The porosity of the active particles could be as high as 60% with the voids typically filled with electrolyte. Even though precise measurements were not taken, no visible increase in the lateral dimension of the specimen was observed. This suggests a very low Poisson ratio of the cell material for which a model of compressible foam could be used in the first approximation. In other words an almost uni-axial strain state was created in the tests. It is seen that the pouch cover provides some constraint to the deforming material so that the resulting force-level is slightly higher. It is seen that Mylar casing contributes very little in this lateral compressive direction. From the raw data on a bare cell shown in Figure 18 above the relationship between stress and volumetric strain was extracted, where the volumetric strain uses an engineering measurement. This data is presented below in Figure 19.

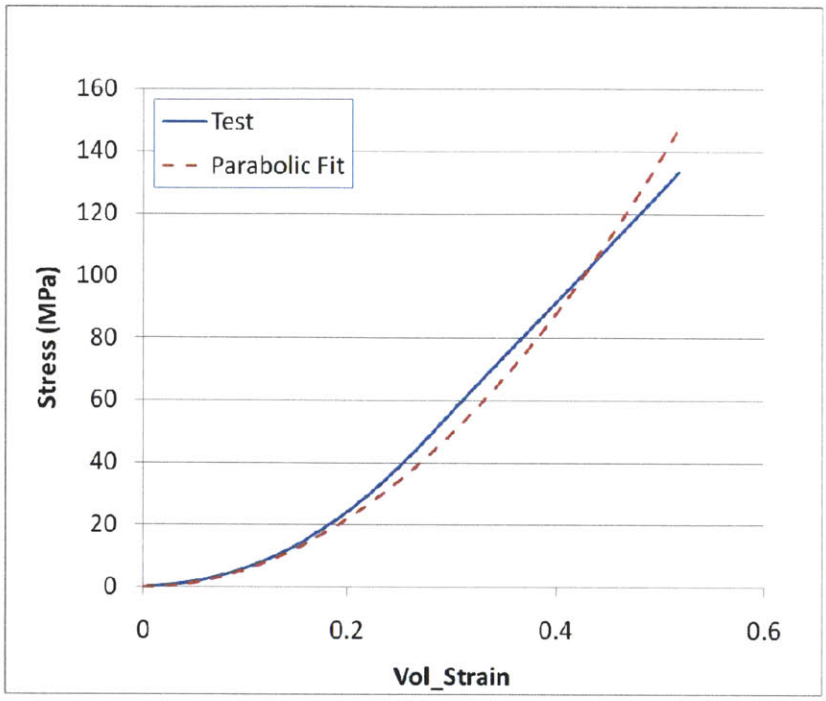

Figure 19 Experimental Stress-Volumetric Strain Curve for Bare and Pouched Cells

The above measured relation between the stress and the average engineering strain provides the basis for subsequent numerical simulation. In addition to the average through-thickness properties, the strength of individual components was measured by performing compression tests of the stacks of identical current collectors (one stack each of aluminum and copper) and separator. The measured load-displacement curves of the individual components are shown below in Figure 20. The determination of the strains of individual components from the displacement and thickness measurements is described in Section 4.1. An interesting method of determining the cohesive and friction constants of the Coulomb-Mohr model of electrode material from the nano-indentation tests was developed in Gannuau et al 2006 (18). Also, a fascinating procedure to measure the elastic properties of the electrode active material under different percentages of charge was reported in Deshpande et al 2010 (19). The accuracy of the present measuring technique does not allow the precise determination of the elastic modulus, which is important in simulation of the buckling problem.

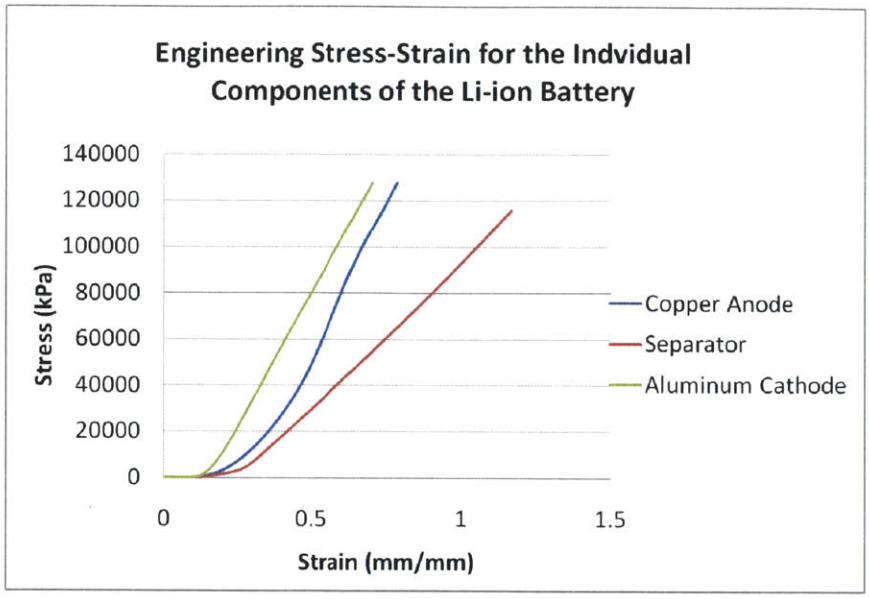

Figure 20 Engineering Stress Strain for the Load-Displacement Curve of Cathode, Separator, and Anode

6.3 Lateral Indentation of the Cell by a Hemispherical Punch

For this experiment the radius of the hemispherical punch was chosen to be R=6.35mm, which is comparable to the thickness of the cell. It is thought that such geometry represents a more realistic scenario of a foreign-object intrusion into a battery. The measured load-displacement relation for bare and pouched cell is shown in Figure 21 below.

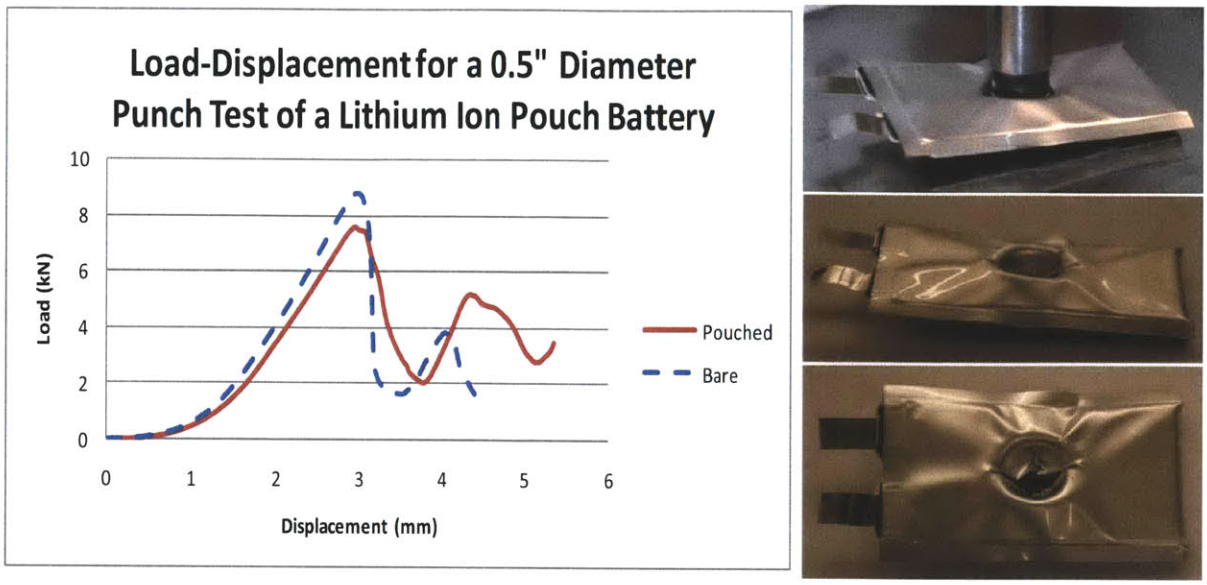

Figure 21 Measured Load-Displacement Curve for Hemispherical Punch Indentation (left) with Photographs of Damaged Cell (right)

There was little difference between the force level of pouched and bare cells. Bare batteries allowed observation of the interior over the experiment. During the test, a progressive fracturing and delamination of subsequent layers was observed. At the punch travel of approximately 3mm, the load dropped indicating internal failure. Upon inspection there was a clear hole punched through a sizeable portion of the thickness of the cell. It was difficult in this test to detect the actual onset of first rupture of the separator which would have caused an electrical short-circuit and possible thermal events. Future tests of partially discharged batteries will allow detection of a voltage drop which will indicate the exact point of electrical short-circuit. The indentation test of the bare cell produced a progressive delamination, circumferential buckling, and rising of the individual layers. The test of the cell confined by the pouch did not exhibit this phenomenon. The results of the punch indentation test were used for validation of the constitutive model developed during the lateral compression test.

6.4 Unconfined Axial Crush of the Cell in the Width and Length Direction

Again, both bare and pouched cells were tested in the wide-column buckling configuration. Compression tests in the width and length direction will be described separately. These axial crush tests required the use of a retention device which prevented the cells from sliding to the side. Providing this was an aluminum plate with a rectangular groove machined to the thickness of the cell, Figure 22 below. In this type of test dramatic differences in force levels were noticed for the bare versus pouched cells.

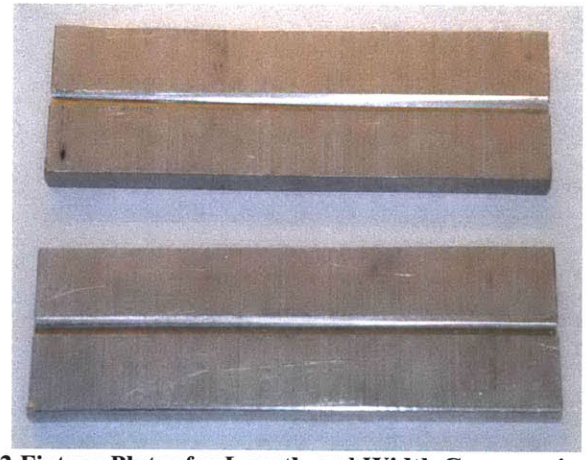

Figure 22 Fixture Plates for Length and Width Compression of Cells

Compression in the Width Direction. As shown by Figure 23 below, the cell with the outside Mylar cover underwent nearly linear compression like a perfect column up to a force magnitude of 250N followed by a sudden compression/shear buckling after which most of the strength was lost. In contrast, the bare battery followed a non-linear pre-buckling path for which the maximum load was only 80N after which a "plastic" hinge-mechanism developed leading to a decaying post-failure response. The displacement to peak load curve was different in both cases. Some delamination was observed in the bare column. Altogether the strength of the pouched battery was six times greater than that of the bare battery.

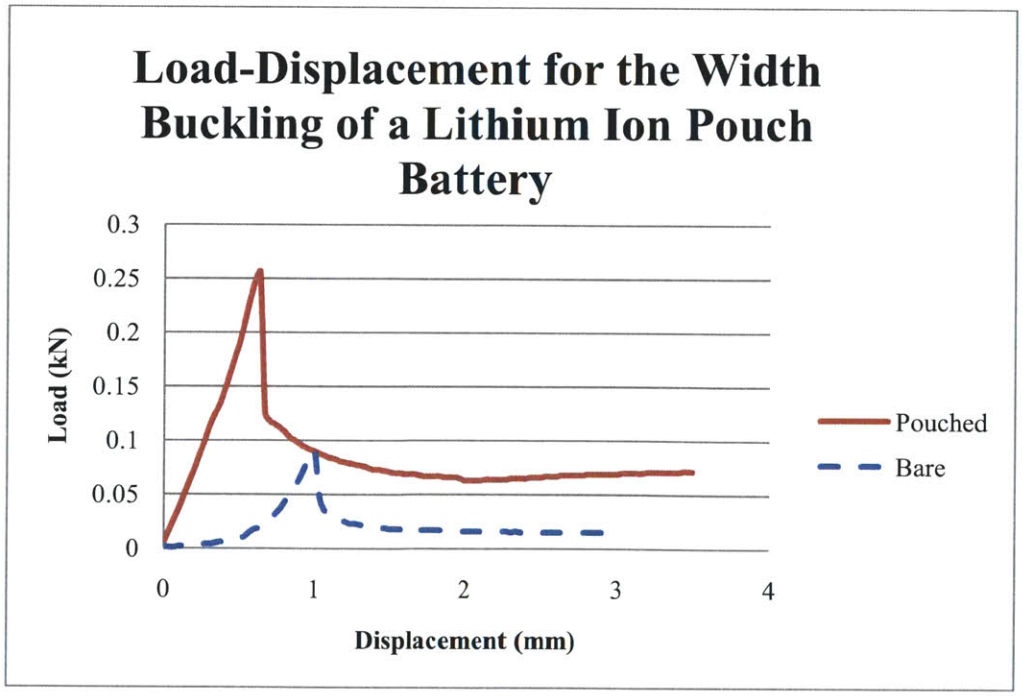

Figure 23 Load-displacement Response of Bare and Pouched Cells Compressed in the Width Direction

Compression in the Length Direction. The sequence of events was similar to the previous case; however, there was almost an order of magnitude smaller pre-buckling modulus, as shown in Figure 24 below.

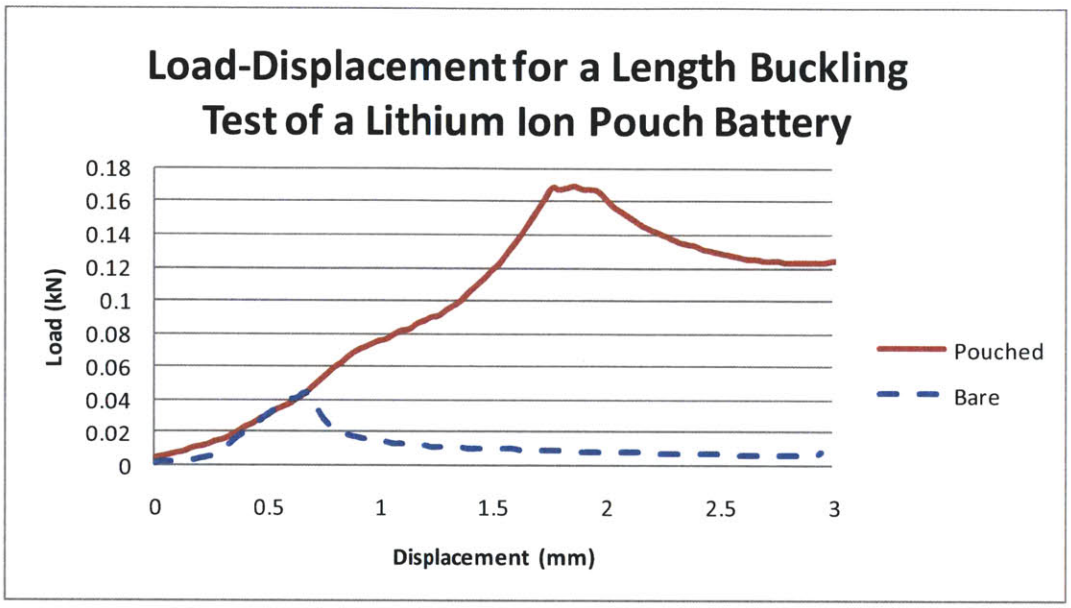

Figure 24 Load-displacement Response of Bare and Pouched Cells Compressed in the Length Direction

The buckling of the bare battery also produced a very visible delamination along the plane of symmetry of the cross-section, as shown by Figure 25 below. While the buckling of the bare vs. pouched battery initially follows the same curve for the length buckling, the bare battery buckled much earlier, as evidenced in Figure 24 above. The results of the above test provide an important clue to the successful design of the compression tolerance cells by choosing a suitable type of outside casing such as Mylar, plastic, aluminum, plastic, composite, steel, etc.

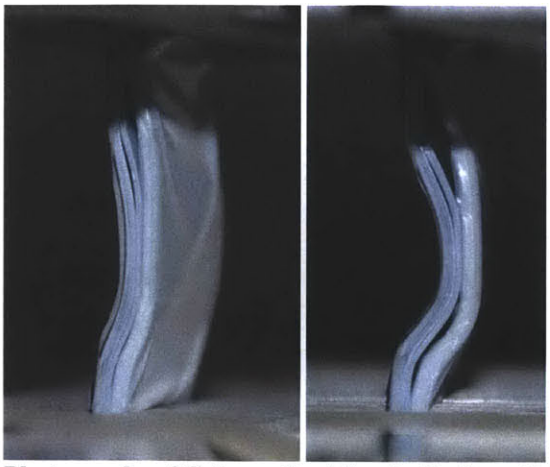

Figure 25 Photographs of Column Buckling in the Length Direction

6.5 Confined Compression Test of the Cell in the Width Direction

Only bare cells were tested in a special fixture shown in Figure 26 below.

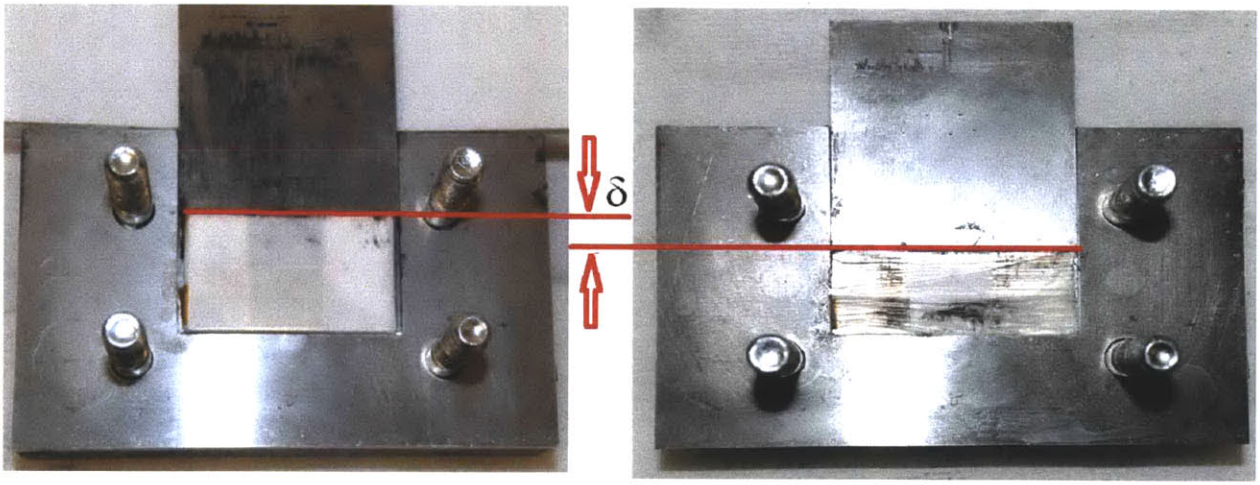

Figure 26 Fixture with Battery for Confined Compression Test in the Width Direction, before and after Test, with Cover Plate Removed

Great care was taken in tightly fitting the fixture around the cell to minimize extrusion of cell material between adjoining faces of the fixture. The maximum travel of the punch was 13mm. Electrolyte was observed to leak quite early in this test, indicating that the change in volume was partially due to escaping electrolyte from the porous media. Initial runs with the device gave erroneous data which was later attributed to the friction developed by the tightly fitting plate. This was resolved by the use of spacers, lubricant, and re-maching surfaces for tighter clearances. Subsequent tests on an empty fixture resulted in negligible amounts of friction developed.

A considerable force of up to 60kN was reached during this test. Further pressures would have resulted in extrusion of cell material. A photograph of the cross-section of the battery corresponding to the maximum punch travel is also shown in Figure 27 below. At this stage, short wavelength buckles develop in an analogy of Euler column buckling on elastic foundation. The number of buckles along the length is 16. It would appear that the layers at the center of the battery have buckled first and subsequently brought the entire cross-section of battery into wave-like deformation. Similar deformation patterns were observed under compression of high-density honeycomb, Baker et al (18).

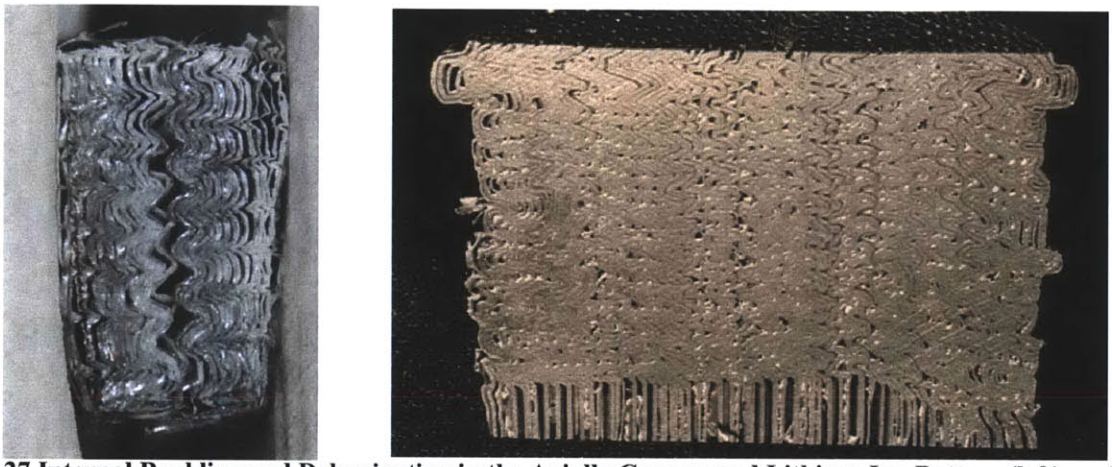

Figure 27 Internal Buckling and Delamination in the Axially Compressed Lithium-Ion Battery (left), and High Density Aluminum Honey Comb (right), Baker et al, 1998

The load-displacement data was converted into stress-strain curves and compared to the one generated from the lateral compression. The stress-strain curve is shown below in Figure 28. In both cases the state of strain was almost uni-axial and therefore, the comparison reveals the contribution of the aluminum and copper foil to the response of the system. In the lateral compression, the layers of the foil are normal to the loading direction and therefore do not contribute to the strength. In the present axial compression the layers of the foil are positioned along the direction of loading. The difference between the stress-strain curves obtained from lateral and axial compression is quite distinct in Figure 28 below. The difference is due to the buckling of multiple layers of foil. This process can be modeled using a classical solution of a buckling beam on foundation (19), see section 7.6.

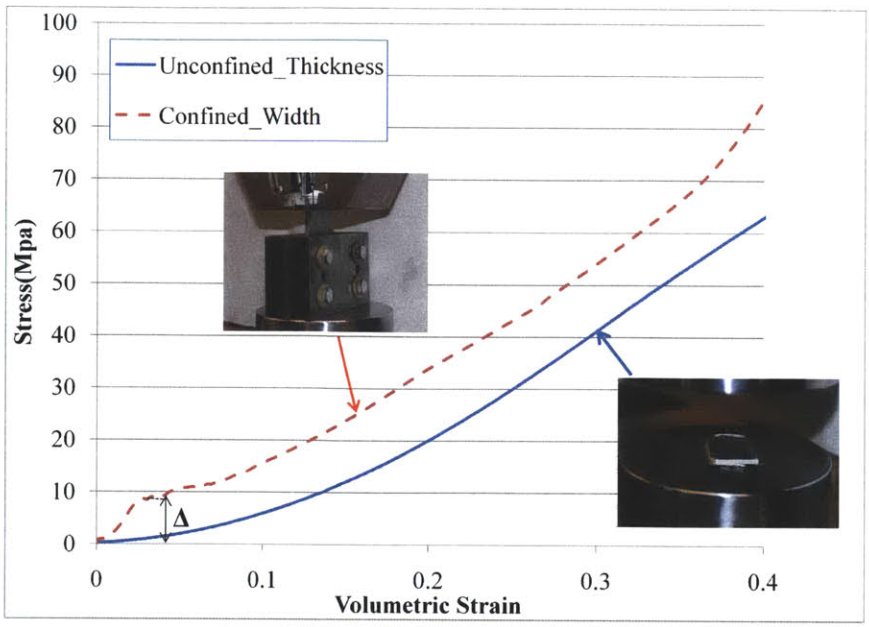

Figure 28 Stress Strain Curve for Confined Compression in the Width Direction Compared to Unconfined Compression

6.6 Three Point Bending Test of a Medium-Sized Cell

A medium-sized cell was chosen for this test as the larger size allowed the use of a particular 3-point loading fixture available to the lab, see Table 1. The radius of the roller support was 15mm while the radius of the loading cylindrical punch was equal to the thickness of the cell which was 8mm. The distance between supports was 95mm with an overhang of 10.8mm. As before, tests were conducted with and without the pouch covering. No local through-thickness indentation was observed. The tests of cells with and without pouch produced entirely different results. The battery with Mylar casing behaved as a regular simply-supported beam undergoing three-point bending. A photograph sequence of this test is shown below in Figure 29. The fold developed in the shell casing on the compressive side leading to the shift of the neutral axis and the corresponding drop in the bending capacity of the center section. As a result a plastic hinge developed under the punch with a straight section on both sides.

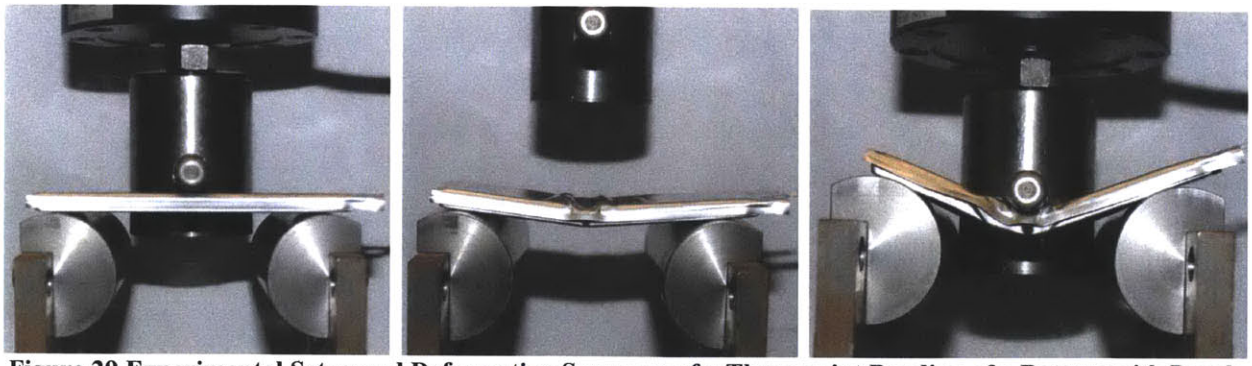

Figure 29 Experimental Setup and Deformation Sequence of a Three-point Bending of a Battery with Pouch

In the subsequent test the pouch casing was removed and the bare battery was placed in the same fixture. Here the deformation mode resembled that of a clamped beam even though it remained simply-supported, Figure 30.

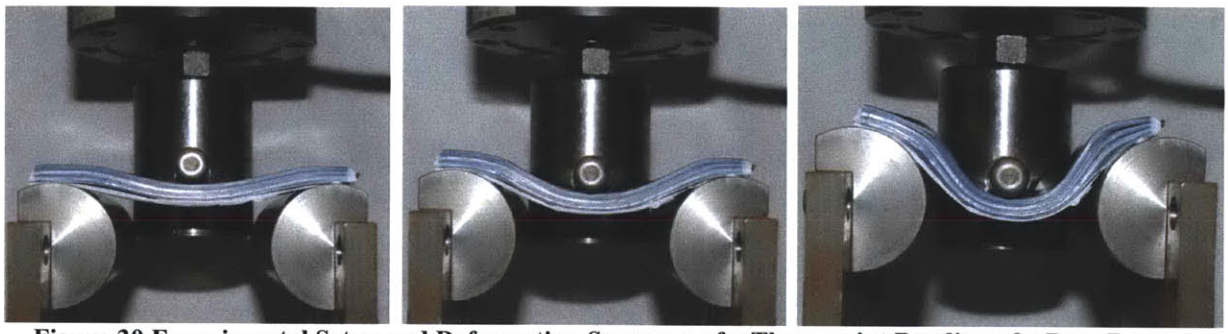

Figure 30 Experimental Setup and Deformation Sequence of a Three-point Bending of a Bare Battery without Pouch

This was the most unexpected and bizarre observation of the entire experimental program. The full explanation would entail a very detailed analysis of the delamination process and interactions including the effects of the friction between layers of electrodes and separator. A simpler qualitative explanation is provided in the Section 7.7. The comparison of the load-displacement relation for the pouch and bare battery is shown below in Figure 31. In order to prevent sliding of the ends from the supports the punch travel was limited to 25mm.

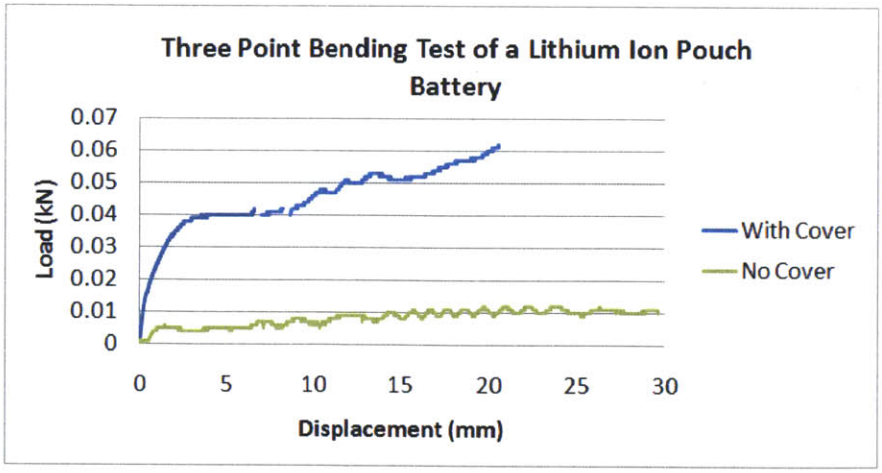

Figure 31 Comparison of Measured Load-displacement Curves of Pouch and Bare Cells Subject to 3-pt Bending

The strength of the pouch battery is shown to be 5 times larger than that of the bare cell. These graphical results alone underscore the vital importance of designing a proper shell-casing for any type of battery.

7. Derivation of Closed Form Solutions for Cylindrical and Prismatic / Pouch Batteries

7.1 Analytical Solution of Lateral Crush by Rigid Cylinder

In order to predict the strength and deformation of the battery cell in different load scenarios a suitable constitutive model of the jelly roll is required. There are two possible approaches to develop such a model. One is to consider the jelly roll as a laminated composite and estimate the material properties based on the properties of a system of individual layers of active electrodes, electrode collectors, and the separator. This approach will be pursued in the course of the new MIT consortium on modeling and safety of lithium ion batteries (22). The other method is to consider the jelly roll as a homogenized material and estimate the properties based on physical testing the whole cell by extending the analytical solutions developed earlier by Wierzbicki et al 1988 (23). The second method is adopted for this study, as it is considerably more time-efficient in terms of model development and FE simulation time. It also gives a reasonably accurate prediction of the behavior of the cell. This study uses extensive testing of the battery cell and jelly roll of a commercially available 18650 lithium-ion cylindrical cell, combined with the use of analytical solutions to estimate the material properties of the cell and develop the subsequent finite element model. Such a model of a single cell can then be used to develop finite element models of different battery modules and ultimately the entire battery pack can be coupled with finite element models of the whole vehicle. It also will provide history of stress and strain in the representative volume element which is needed in multi-scale modeling of the cell to study micro-scale behavior of the electrode/separator assembly.

7.2 Analytical Solution for the Crush Behavior of an Empty Shell

The crushing strength of a cell comes from both the strength of the outer shell casing and the crush-resistance of the interior core winding. The analysis of the empty shell casing is presented first. Closed form solutions of a thin cylindrical shell with and without end caps will be reviewed under two types of loading: lateral indentation by a rigid rod and lateral compression between two plates.

The static and dynamic response of a thin pipe subjected to a rigid punch loading was studied in a series of publications by one of the present co-authors (23; 24; 25; 26; 27). The solution that would be most useful to the present problem refers to the resistance of the free end cylinder subjected to lateral knife type of loading. The relationship between the indentation force F and the indentation dept δ is given by:

$$F_{shell} = \sigma_0 t^{1.5} \sqrt{2\pi\delta} \qquad (1)$$

where σ_0 is the average flow stress of the material of the shell casing, which was determined in the previous section and t is the thickness of the shell. The above equation is valid in the range of the punch travel not greater than the radius of the shell. It should be noted that the radius of the cylinder does not enter in Equation 1. The accuracy of the above solution was shown in the literature to compare well with full scale and component tests of pipes subjected to wedge type of loading. Finite element simulation was run assuming the lateral punch to be of a circular rod shape. Comparison between the numerical solution and Equation 1 presented in Figure 32 below shows a very good agreement.

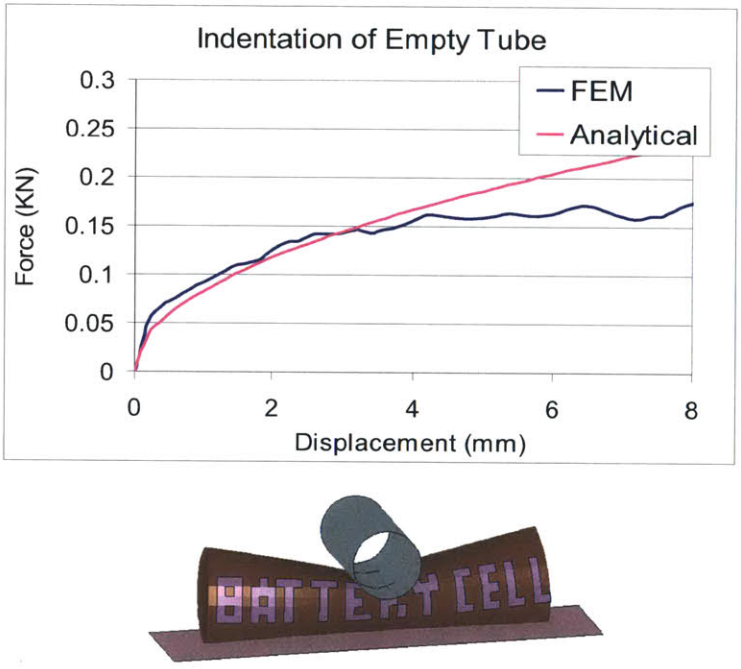

Figure 32 Comparison of finite element simulation and closed form solution (Equation 1) for an empty shell loaded by a rigid rod

The second problem of interest to this study is a lateral crushing of an empty tube with end caps removed between two rigid plates. We adopt here a very realistic closed form solution of this problem derived by Runtz and Hodge (28). The crushing force is related to the crush distance through the following equation:

$$F_{yshell} = \sigma_0 t^2 \left(\frac{l}{R}\right) \frac{1}{\sqrt{\left(1-\left(\frac{\delta}{R}\right)^2\right)}} \qquad (2)$$

where l and R are the length and radius of the battery, respectively. Comparison between the above simple closed form solution and the numerical simulation, presented in Figure 33 below shows a good agreement, except the initial phase when the contact between the plate and the cylinder is established. Also, the deformed shapes of the empty shell are almost identical in analytical and numerical solutions.

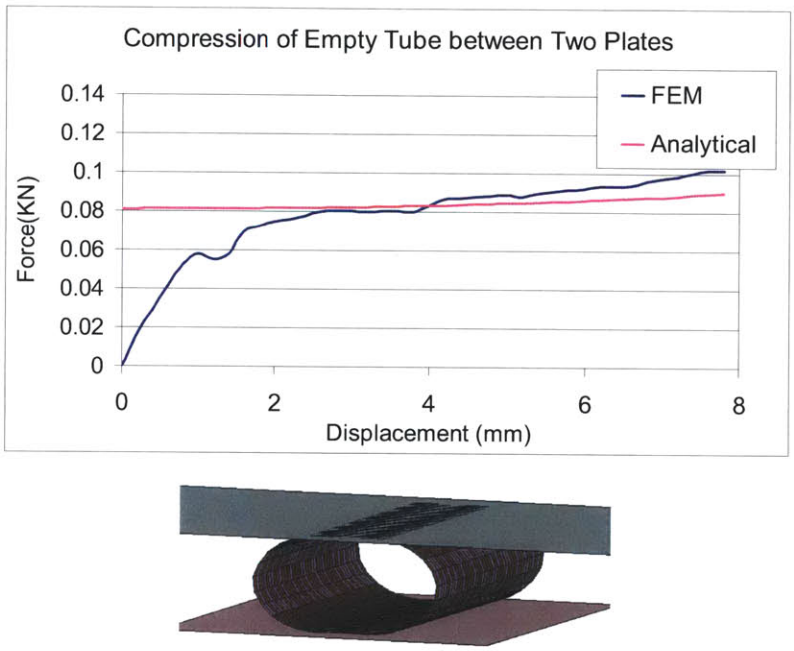

Figure 33 Finite Element vs Analytical Solution for Lateral Compression of an Empty Shell

It can be concluded that the good accuracy of the above two analytical solutions makes them especially useful for developing a constitutive model of a battery cell consisting of both the jelly roll and shell casing.

7.3 Analytical Solution for the Complete Cell (Outer Shell + Jelly Roll)

The determination of the constitutive model of the jelly roll is the most critical section of the entire paper. The approach taken here is to determine the parameters of the assumed constitutive model from one test and then verify the model by comparing numerical prediction with the remaining two types of tests. It was decided to use the test on lateral indentation by the rigid rod for model identification. The jelly roll in the

simplest approach will be described as an isotropic homogenized material. To estimate the material properties of the homogenized material model for the jelly roll, a methodology is developed combining the input from rigid indentation crush test with an analytical solution. In this section, the analytical model for indentation of the battery cell is explained in detail. The verification will then be performed for two problems: lateral compression of a battery cell between two plates and axial crush. Both test results are available.

The previous solution for the crush behavior of shell casing can now be extended to include the contribution of the jelly roll. The total magnitude of the crush force F_{test}, (which is measured in the test) is the sum of the resistance of the outside shell casing F_{shell} and the jelly roll, F_{jelly}.

$$F_{test} = F_{shell} + F_{jelly} \tag{2}$$

where the expression for F_{shell} was derived in Section 7.2, Eq (1).

From the geometry of the problem, the projection of the contact area between the rigid rod and the cell assumes an elliptical shape, where a, b are the major and minor axes of the ellipse. It is assumed that the resisting stress, $\sigma(\delta)$ of the jelly roll is spatially constant over the elliptical area, but variable with amount of crush distance, δ. Few types of material would satisfy this requirement. One is a simple elastic-perfectly plastic material idealization. However, this material assumes incompressibility. From the experimental observation on the three types of test described in Section 5, there was clear evidence that the jelly roll material has been compressed. An alternative model is that of a high density foam which admits compressibility. This model is adopted in the present investigation. According to the above discussion:

$$F_{jellyroll}(\delta) = \pi a(\delta) b(\delta) * \sigma(\delta) \tag{3}$$

where from the geometry of the problem, shown in Figure 34, one can show that :

$$b = R_{ind}\sqrt{1-(1-\frac{\delta}{R_{ind}})^2} \tag{4}$$

In which R_{ind} is the radius of the rigid rod. Furthermore, the assumption of inextensibility of the material in the circumferential direction yields:

$$a = \frac{\pi\delta}{4} \tag{5}$$

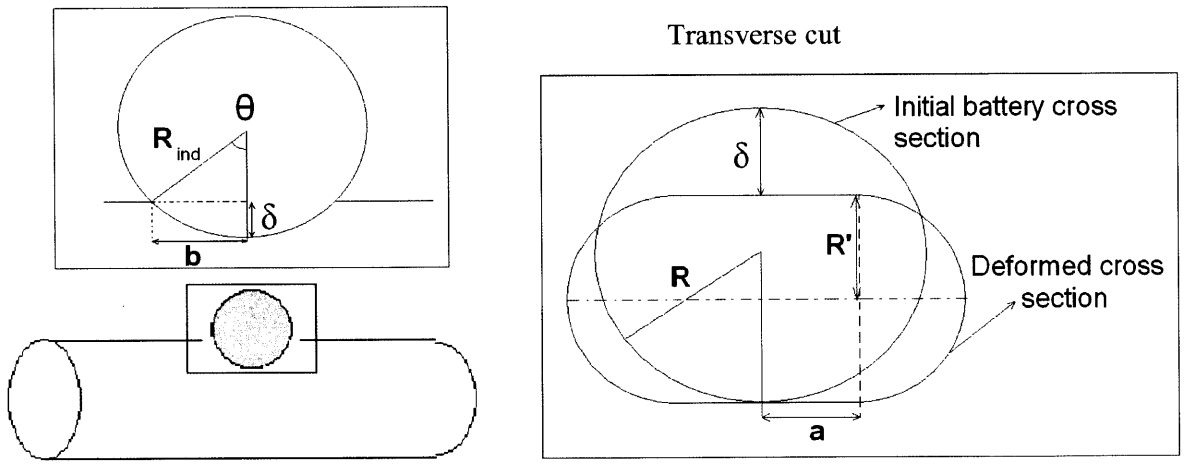

Figure 34 Assumed geometrical model of the indentation process

Combining Equations 2 and 3, the resisting stress can be calculated as:

$$\sigma(\delta) = \frac{F_{test}(\delta) - F_{shell}(\delta)}{\pi a(\delta) b(\delta)} \tag{7}$$

where all terms in Equation 7 are known functions of δ.

The model of the foam requires as an input the relation between stress and volumetric strain. The resisting stress as a function of dept of indentation is given in Equation 7. The relation between the volumetric strain ε_v and the indentation dept can be estimated using the definition of the volumetric strain taken at the plane of symmetry:

$$\varepsilon_v = \frac{A_0 - A}{A_0} \tag{6}$$

where $A_0 = \pi R^2$ is the initial area of the cross section. The current cross sectional area can be calculated from the geometry shown in Figure 34, and is equal to $A = \pi R'^2 + 4aR'$. The final expression for the volumetric strain is:

$$\varepsilon_v = \frac{\delta^2}{4R^2} \tag{7}$$

All the data now exists to calculate the relation between the stress and volumetric strain for the foam model. This is shown in Figure 35.

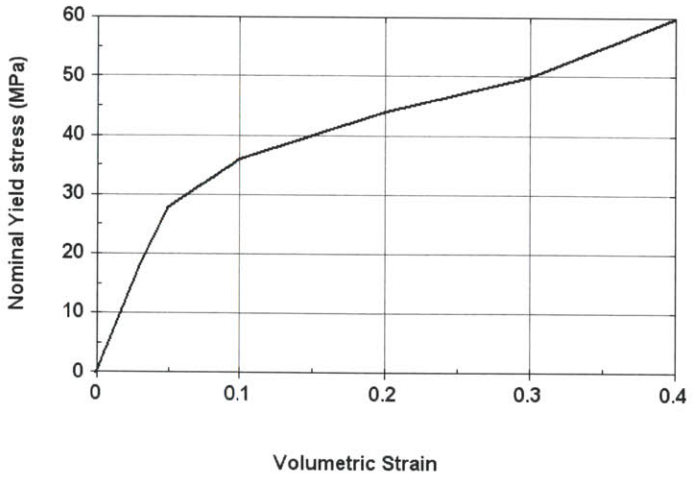

Figure 35 Yield stress versus volumetric strain of the jelly roll

The stress range is relatively wide up to 60 MPa. Typical stress resistance of polyurethane and aluminum low density foams is of an order of 3-5 MPa. The strength of the foam is related to its density. Therefore, the present foam should be classified as high-density foam.

7.4 Analytical Comparison of Prismatic / Pouch Cell in the Thickness Direction

Each of the five layers of the traditional battery structure is made of different materials. The properties of the cathode and anode current collectors as well as the Mylar pouch material are taken from open literature and provided in Table 4 below:

Table 4 Material Properties of Foils

	Aluminum Foil	Copper Foil	Mylar (gage 500)
Yield stress (MPa)	180	210	-
Ultimate stress (MPa)	195	230	180
Yield strain	0.017	0.022	-
Elongation (%)	2.7	3.5	-
Young's Modulus	70	110	3.45

(GPa)			

The Young's Modulus of aluminum and copper foils are an order of magnitude higher than those of the remaining layers (active material and particles). Therefore, under the generated stress levels, the compressive strain in the foil, ε_{Al} and ε_{Cu}, can be neglected.

From the measured load-displacement data, P-δ, one can calculate the engineering stress σ by dividing the total force by the original area and the average compressive strain ε_{Av}. Let us denote by h_1, h_2, and h_3 thickness of the anode, cathode, and separator, respectively. Then the strain averaged over the three layer assembly is:

$$\varepsilon_{Av} = \frac{\delta}{N(h_1 + h_2 + h_3)} \tag{10}$$

where N is the number of periodic layers in the thickness direction. Because in the lateral compression test the unixaixal strain prevails, the measured strain is the volumetric strain. The volumetric strain is usually expressed in the logarithmic measure; for the present qualitative analysis the engineering strains are used. The stresses are the same in all layers but the strains differ in general from layer to layer. For the purpose of developing the constitutive equation of the Representative Volume Element (RVE), the present text provides information as the average strain is measured in the thickness direction. The relationship between the individual strain ε_1, ε_2 and ε_3 in the respective layers and the average strain is:

$$\varepsilon_{Av} = \varepsilon_1 \frac{h_1}{h_1 + h_2 + h_3} + \varepsilon_2 \frac{h_2}{h_1 + h_2 + h_3} + \varepsilon_3 \frac{h_3}{h_1 + h_2 + h_3} \tag{11}$$

For a homogeneous material, $\varepsilon_1 = \varepsilon_2 = \varepsilon_3 = \varepsilon_{Av}$.

The present test provides data on the compressive strength of the electrode / separator system. In the scale of the battery pack and module, one can envision mostly compressive types of load, however buckling of batteries results in both tension and compression zones.

There is a general understanding that the current lithium polymer batteries are constructed as very weak composites consisting of layers of foils and separator sandwiched between carbon oxide particles and held together by a polymer (binder). The tensile and compressive forces of the electrode / separator assembly are then controlled to a large extent by the strength of the binder. Liu et al presented a concept of reinforcing the active electrode material by carbon fibers and then replacing the liquid electrolyte with solid-state polymer electrolyte (29). They have demonstrated that the above modifications increase the

tensile strength of the cathode by almost an order of magnitude. Likewise, the compressive strength of the electrode should also increase by a similar ratio. This present paper is a first step in providing manufacturers with suitable tools for designing batteries with increased structural performance.

7.5 Punch Indentation of a Prismatic / Pouch Cell

The punch indentation test is relatively simple, does not produce exceedingly large forces and provides a wealth of information relevant to the task of modeling the layered structure of batteries. There is an axi-symmetric stress state under the punch, where through-thickness compressive stresses σ_{ZZ} and shear stress σ_{RZ} are dominant in the active crushable material. The thin layer of foil is subjected to predominantly tensile stresses σ_{RR}. The closed form solution of the punch-indentation problem is presented in this subsection.

The present approach is valid for any given stress-strain relation of the compressible active powder. For simplicity, a parabolic fit is used, $\sigma = A\varepsilon^n$, to describe the uniaxial stress-strain relationship of the active material with binder. Aluminum and copper foils exhibit little hardening and can be modeled as rigid perfectly-plastic material with the flow stress σ_o. The fully calibrated multi-axial response of the active material with binder is currently lacking. Therefore, the approximate solution will be derived in this paper by conserving only the axial (through-thickness) stress σ_{ZZ} and neglecting shear stress σ_{RZ}. A more complete derivation with a full iteration between σ_{ZZ} and σ_{RZ} is presented in Wierzbicki et al (30).

The vertical displacement of the material points under the punch *w(r,z)* in the cylindrical coordinate system (r,θ,z) is approximated by the following function:

$$w(r,z) = \delta \frac{z}{H}\left[1 - \left(\frac{r}{r_1}\right)^2\right] \tag{12}$$

where H is the thickness of the battery cell and r_1 is the outer radius of the contact between the punch. For small indentation depths, $r_1 = \sqrt{2\delta R}$, where R is the radius of the hemi-spherical punch. It is further assumed that the trajectory of all material points are vertical such that the radial components of the displacement field vanishes, $u_r=0$. The above displacement field satisfies all kinematic boundary conditions. Engineering strains are used to calculate axial and radial strains in the powder material from the assumed displacement field. Tensile strains in the foil ε_{rr} are derived from the nonlinear Lagrangian definition. The expression for the total resistance of the N layers of foil is:

$$P_{foil} = \frac{2}{3}\pi\sigma_o h N \delta \tag{13}$$

where h is the thickness of a single foil. The resistance of the remainder of the battery material, P_{powder}, (without foil) is given by:

$$P_{powder} = \frac{\pi}{2} A \frac{R}{H^2} \delta^3 \tag{14}$$

The total punch force P is calculated by adding the resistance of active powder material and foil, $P = P_{powder} + P_{foil}$.

The above solutions were plotted for the following measured values of material and geometrical parameters:

A (N/mm)	R (mm)	H (mm)	σ_o (N/mm^2)	h (mm)	N
500	6	48	200	0.025	46

and the result is:

$$P = 0.3\delta^3 + 0.5\delta \tag{15}$$

Comparison between the analytical prediction and experimental load-displacement curve is shown below in Figure 36. The closed-form solution identifies all geometrical parameters of the cell. The foil material is well characterized by the average low stress σ_o. The active material with binder is described by the amplitude A of the quadratic power law. The strength of the separator is of the same magnitude as that of the powder and is therefore lumped in the constant A. The above solution can be used for a preliminary design of batteries from the point of view of indentation by a foreign object. Combined with simple indentation test in a cell, they also serve as a rapid determination of the uniaxial stress-strain curve of the coated material.

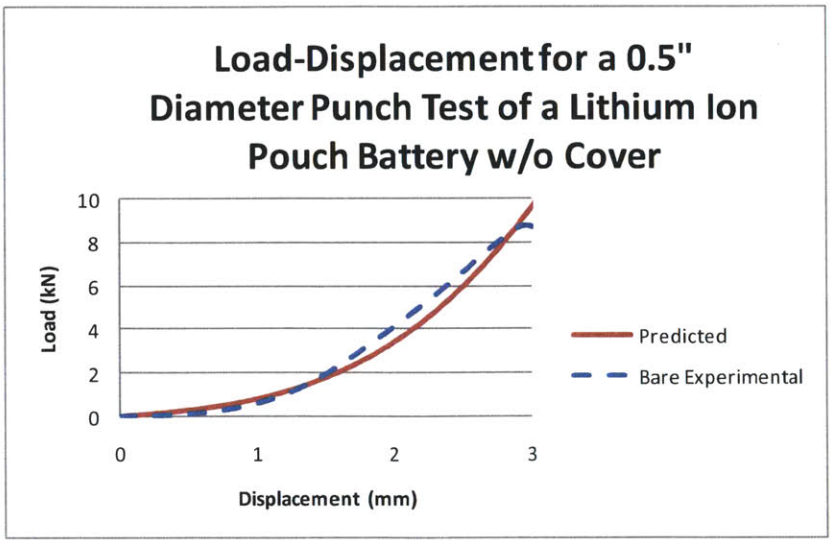

Figure 36 Analytical vs Experimental Load-Displacement Curve for Punch Indentation of a Bare Battery

7.6 Confined Compression of a Prismatic / Pouch Cell

The tests on confined compression of a bare cell in the thickness and width directions give rise to a uniaxial strain in the both cases. And yet the calculated stress-strain curve, shown in Figure 28 (earlier), is markedly different. The layers of foil act in series in the through-thickness compression and because of the incompressibility of metallic material do not contribute to the strength. Foil sheets are arranged in parallel to the loading direction in the compressive direction along the width and add up to the strength of the composite. Both curves diverge early on, at in-place displacement of less than 0.025mm, and then stay parallel for the remainder of the process. The compressive strain in this early stage is less than 0.001 so the aluminum and copper foils respond in the elastic range.

The difference in the stress level can be explained and further quantified by the response of a beam on elastic foundation. The initial pre-buckling slope of the perfect column is $^{Et}/_{lh} = 833\ ^{N}/_{mm^2}$. The actual measured slope is half of this value indicating a fair amount of out-of-straightness imperfections. A simply-supported Euler column buckles in the fundamental mode. The presence of foundation causes the column to buckle with higher modes, according to:

$$k = D(\frac{n\pi}{l})^2 \qquad \textbf{(16)}$$

where n is the number of half waves, k is the foundation constant, and D is the bending rigidity of thin foil, $D = \frac{Et^3}{12(1-\nu^2)}$

The textbook solution for the buckling load per unit width of a single foil is:

$$P = 2D\frac{n^2\pi^2}{l^2} \tag{17}$$

Note, that the foundation constant in the above solution was replaced by the number of buckling waves n, which was measured. The buckling stress is obtained by dividing the buckling load by the separation distance between subsequent layers of foil, $\Delta\sigma_{foil} = {}^{P}/_{h}$. Taking the masured values of n=16, E=90 GPa, l=30mm, t=0.025mm, the additional buckling stress is calculated to be $\Delta\sigma_{foil} = 9.03$ GPa. This value matches perfectly the difference in the two stress-strain curves presented in Figure 28.

The present analysis of tests have identified the length of the local buckling waves in the cell:

$$\lambda = \frac{l}{n} \tag{18}$$

as an important parameter, controlling the mechanical response of the laminated structure of a battery.

7.7 Three-point Bending of a Prismatic / Pouch Cell

Tests on 3-point loading of pouched and bare batteries illustrate the interactive process between individual layers of prismatic batteries. The cell wrapped in the Mylar casing deflected initially as a pin-pin beam with a constant stiffener K. From the solution of the point-loaded beam, the elastic stiffener is:

$$K = \frac{4Ebt^3}{l^3} \tag{19}$$

The above equation can be used to calculate the average elastic modulus of the battery from the measured stiffness K.

From the sequence of loading history (Figure 29 shown earlier), the fold develops in the top face plate on the compressive side leading to a shift in the neutral axis and the corresponding drop in the bending capacity of the center section. As a result, a plastic hinge developed under the punch with a straight section on both sides and the beam suddenly loses its bending capacity. This behavior is both understandable and predictable.

Interesting things are observed in the 3-point bending test. There is a linear variation of the bending moment along the beam with the maximum moment at the mid-span and zero at the support. And yet, the curvature of the beam is reversed resembling that of a fully clamped beam. What invisible reaction moment is causing zero slope at the support? One possible explanation is the presence of friction between apparently unconnected layers. With no friction, the laminated beam deforms as a bundle of

unconnected thin layers where the tension fibers of the top beam are in contact with the compressive fibers of the bottom layers. This gives rise to a length difference at the end points, Figure 37 below. The relative motion with friction imposes additional work ΔW which is proportional to the amount of length difference:

$$\Delta W = \tau t \frac{dw}{dx} \tag{20}$$

where τ is the shear stress $\tau = \mu\sigma_n$developed due to the compressive shear force.

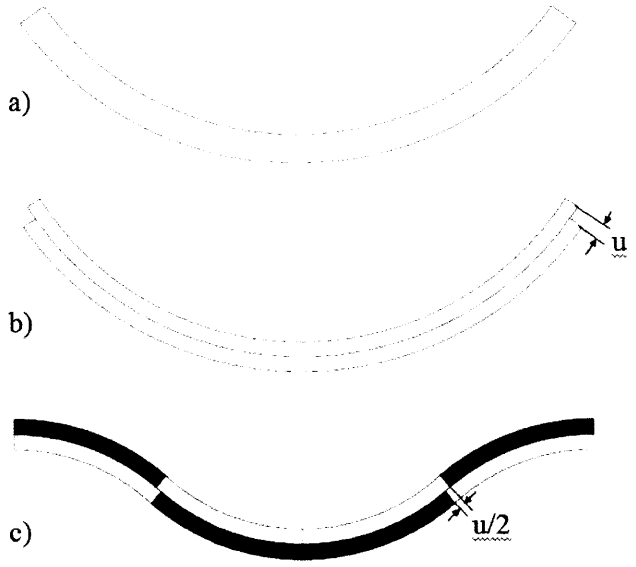

Figure 37 Conceptual Graphs Showing the Amount of Interfacial Slip in Beam with Monotonic and Reverse Curvature

Referring to Figure 37, the work ΔU is reduced by a factor of four if the bent beam assumes the shape of the clamped beam at the same amount of deflection. This analysis underscores the importance and difficulties of modeling the laminated prismatic cell with loosely connected layers.

8. Numerical Simulation of Axial and Lateral Loads on Batteries

8.1 Finite Element Modeling of Cylindrical Cells

A finite element model of the cell was developed in LS Dyna software. The shell casing of the cell including end-caps was discritized using 4-node fully integrated shell elements. The jelly roll was modeled by fully integrated solid elements. The rigid rod and rigid plates were modeled using contact entity from LS Dyna contacts, which assumes a rigid geometrical shape for the contact surface. There were 3108 shell elements and 4560 solid elements in the model. Material piecewise linear plasticity from library of LS dyna materials was used for the shell casing. The following input was used for the model: E=200 GPa, ν=0.3, and σ_{yield}=450 MPa. The effective stress versus effective plastic strain curve was input to the model from the dog-bone specimen test. For the jelly roll, the material crushable foam from library of LS Dyna (Mat 63) was used. The following parameters were used for this model E=600 MPa, ν=0.1, and a "yield" stress versus volumetric strain load curve, shown in Figure 38, was inputted.

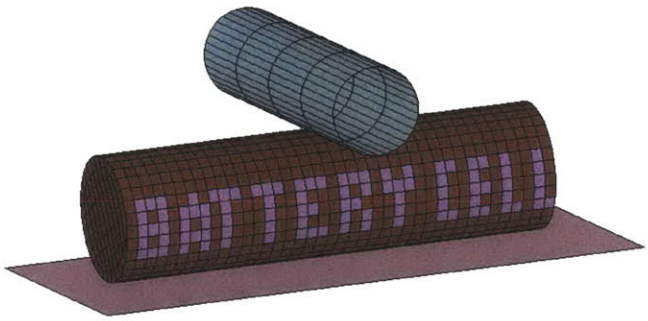

Figure 38 The unreformed FE model of 18650 battery cell

Using 6 CPUs to run the simulation, the indentation simulation took approximately 3 hours. It should be pointed out that the size of FE elements was relatively small (1.5mm in length), which explains the long calculation time.

8.2 Validation of the Cylindrical Model

Three loading scenarios were simulated to validate the material model by comparing the experimentally measured and simulated load displacement curve. This includes indentation by a rigid rod, compression between two plates, and axial crush of the cell. Comparison of the experimental and calculated transient cross sectional shapes was done before in the section dealing with the analytical model.

Indentation by a rigid rod. Figure 39 below shows the comparison of rigid rod indentation simulation with the test. It can be observed that the model was able to accurately predict the load until about 8mm of deformation which is about the radius of the battery cell. That amount of crush is already substantial and any more will seldom be observed in the actual crash tests of battery modules and battery impacts. Therefore, the discrepancy between the physical test and the finite element solution after 8mm crush shown in Figure 39 is of little significance.

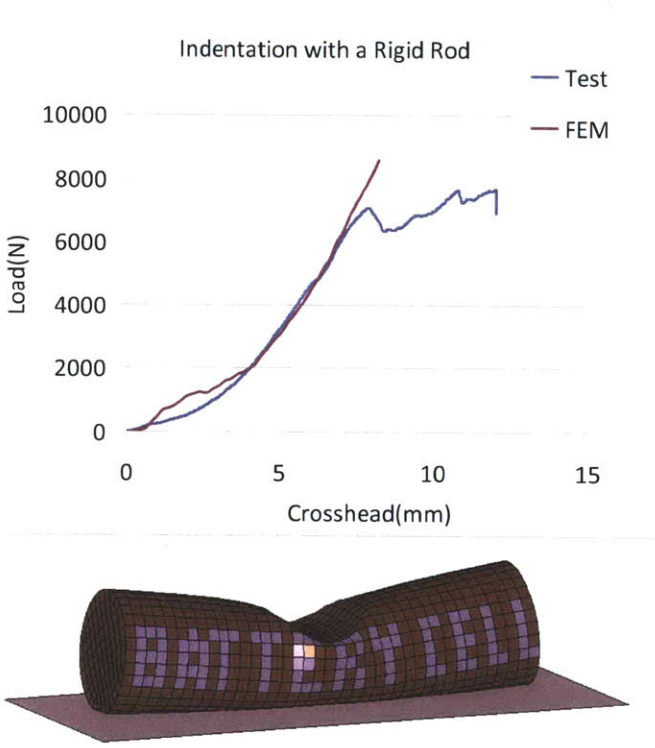

Figure 39 Rigid rod indentation test versus simulation

Compression between two plates. The comparison between measured and calculated load displacement curve for the case of compression of the cylindrical cell between two plates is shown in Figure 40. Again the model predicts the test results quite accurately, until the end of the simulation. It should be noted that both experiments and simulations for this test were performed with no end-caps.

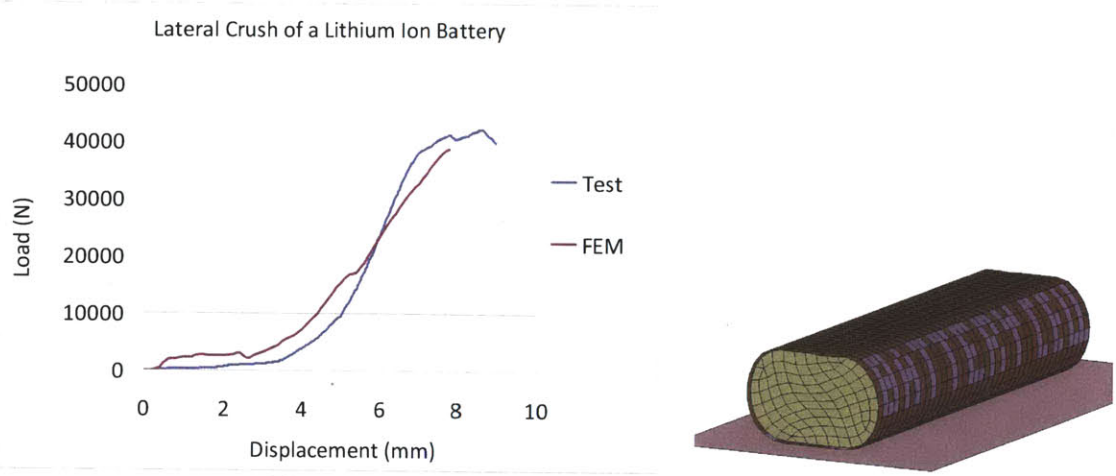

Figure 40 Lateral compression between two plates

Axial Crush. The axially compressed cylindrical cell developed a number of folds clearly shown in Figure 41. Each fold corresponds to a local peak in the load displacement curve. The problem of crash loading of foam filled tubes has been extensively studied at NTNU in Norway (14; 15) and at MIT (16; 17). In this problem, it is more appropriate to compare the absorbed energy versus the crush distance rather than the load displacement curve.

Figure 41 shows the energy absorption of the battery cell during the axial crush in simulation versus test. There is almost a perfect agreement between the two curves which further validates the correctness of this computational model.

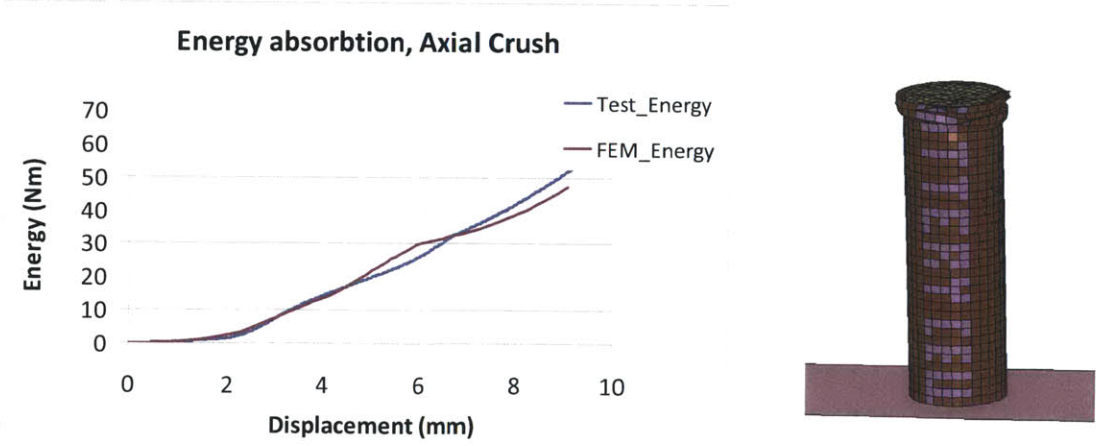

Figure 41 Energy absorption versus the crush distance in an axially loaded cell

LS Dyna version 971 nonlinear finite element software was used for modeling. The finite element model of the cell was constructed in three steps: for the through-thickness compression test, for the punch test, and for the confined compression test.

8.3 Lateral Compression of the Prismatic / Pouch Cell

In the first step the whole cell was modeled using solid fully-integrated elements. A finite rigid wall was modeled under the solid elements. The rigid wall constrains the motion in the Z direction. Also, the reaction force of a rigid wall measures the applied load to the cell. On the top surface of the cell a rigid flat plate is simulated through contact-entity and a uniform motion represents travel of the punch. The displacement was measured from the nodes on the top surface in contact with this plate. The element size in both the length and width direction was 1mm, and in thickness direction, 0.48mm. A crushable foam material from the library of LS Dyna materials was used to model the homogenized behavior of the cell in through-thickness compression. It is believed that the behavior in this direction is mostly a function of the active material and binder properties rather than the aluminum / copper foil or the separator properties, therefore those structures were not modeled for this simulation. The stress-volumetric strain properties extracted from the experiments were applied as the average property for the foam. The modulus of elasticity was calculated from the slope of this curve, E= 500 GPa. The Poisson's ratio was assumed as 0.01, and due to voids in construction of the cell, the material is believed to be fully compressive. Figure 42 below shows the finite element model of the cell and the comparison of load-displacement curve for the model versus the tested cell. It can be observed that the crushable foam model can closely represent mechanical properties of the cell in through-thickness compression tests.

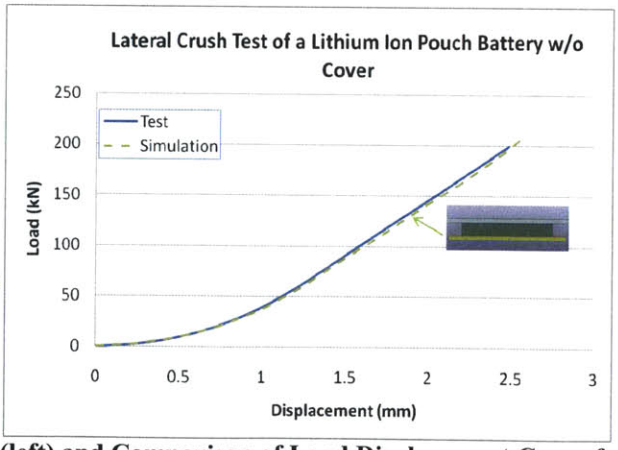

Figure 42 Finite Element Model of the Cell (left) and Comparison of Load Displacement Curve from Simulation to the Test (right)

8.4 Punch Indentation Test of the Prismatic / Pouch Cell

In the next step of modeling the punch indentation test was simulated. This simulation was done in two ways: first by using the same solid element model that was explained in the previous section, and second by introducing four layers of foil which represents the aluminum and copper foils present in the cell. The crushable foam material used for these simulations accepts a tensile cut-off value. This value is very

important for realistic behavior of the cell under hemispherical punch indentation. The average tensile strength of the battery can be calculated from the yield strength of each of its components by using:

$$\sigma_{tensile} = \frac{\sum_{i=1}^{5} \sigma_i \, t_i n_i}{\sum_{i=1}^{5} t_i \, n_i} \tag{21}$$

where i represents the five layers of material in the battery cross section, σ_i is the yield strength of the component, t_i is the thickness of that layer, and n_i is the number of layers. Reports from literature on tensile strength of each layer were used to calculate the average tensile strength. Tensile strengths, σ_i , for aluminum and copper foils are listed in Table 4, for the active anode and cathode particles, σ_i come from the strength of the binder, and can be assumed to be equal. Liu et al, 2008 report on strength of cathodes in tension to be between 2 to 12 MPa, depending on the manufacturing process (27). Dijan et al, 2009 report tensile strength of a Celgard separator to be 60 MPa (28). Considering these values the average tensile strength could be up to 55.58 MPa. This value was used for the solid element simulation, a slightly lower value of 44.4 MPa was used for the simulation with foils, as the foils had partial representation in that simulation. In the second simulation four layers of shell elements were used to model properties of the foils. Two layers were on each side of the cell, and two layers in the middle. The thickness was considered as 0.26mm. Shell elements were 1x1mm in size. A piecewise linear-plasticity material model from library of LS Dyna materials was used to model properties of the aluminum / copper foils. The solid elements were given the same material properties of crushable foam that was explained in the previous section. A rigid sphere of 6.35mm was used to model the hemispherical punch.

Figure 43 below demonstrates the deformation of the cell (solid element model) after the first punch indentation simulation. This simulation is compared with the result of a pouched cell hemispherical punch test, where the pouch prevented delamination of the layers. Simulation also predicts point of failure of the material in this simulation.

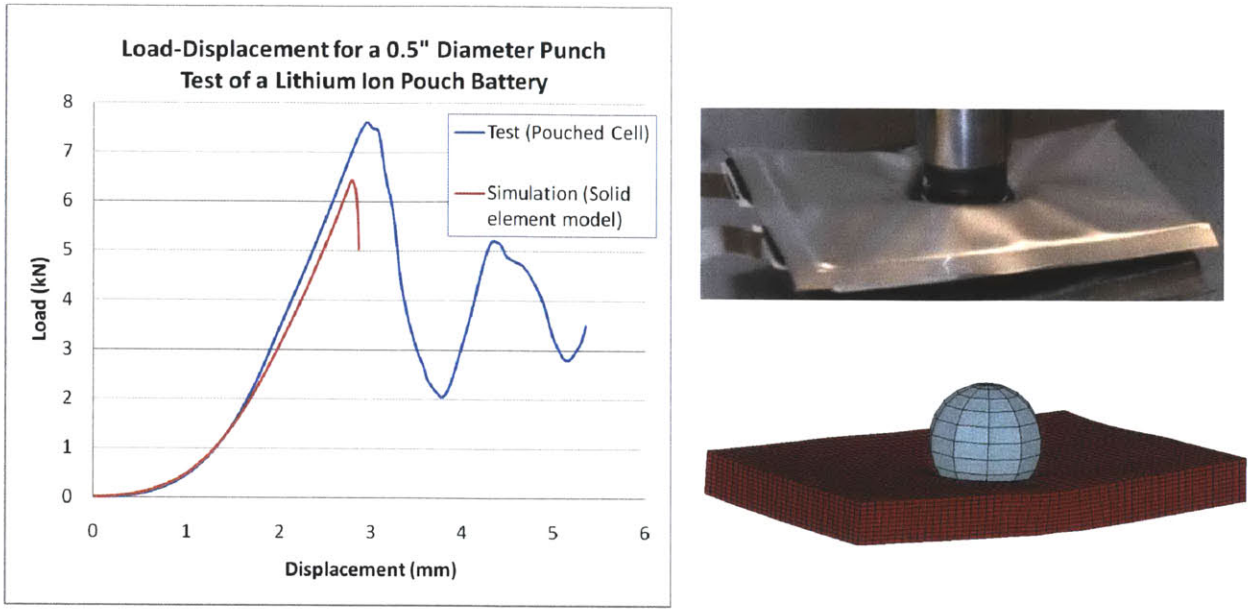

Figure 43 Deformation and Load-Displacement History of the Cell during Punch Indentation Simulation

Figure 44 below shows the second punch simulation (with foils). Also, comparison of force-displacement curve for this simulation against the hemispherical punch test without cover is presented. The simulation closely represented force-displacement behavior of the cell in the punch-indentation test up to the end of simulation. However, the model did not include a failure criterion for the foil. Separation of the top foil layer represents delamination of the cell as observed through the hemispherical punch test.

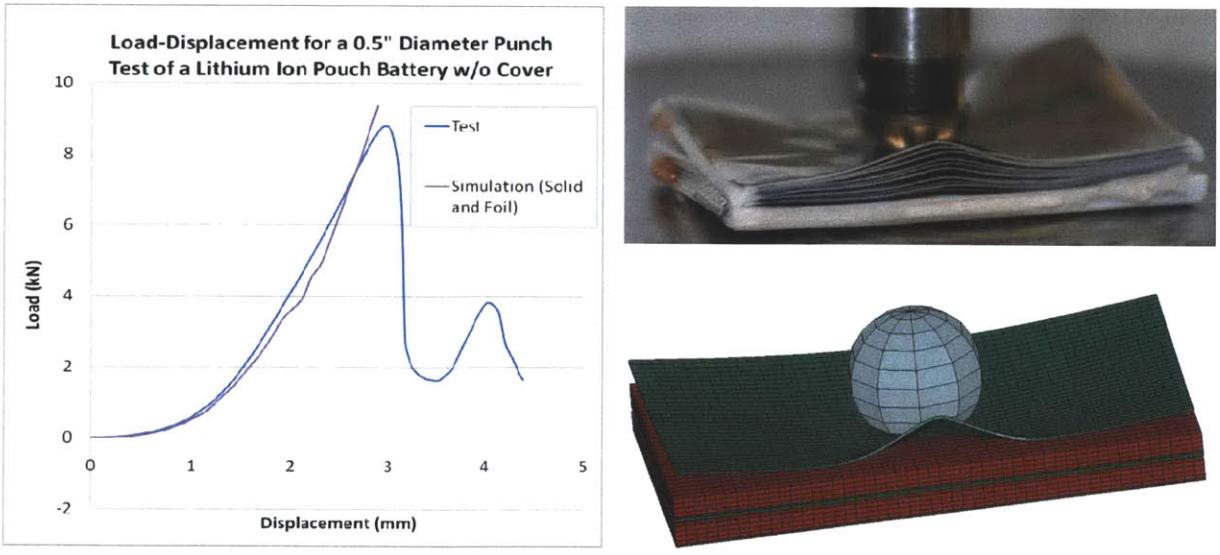

Figure 44 Comparison of Hemispherical Punch Test with the Simulation

The simulation predicts buckling of the faceplate in the width's direction. Clearly the material in the width direction is being drawn inside the created cavity and the in-plane radial displacement produces considerable hoop stresses and leads to buckling. At the same time, the boundary in the length's direction is much further away. The material is not being drawn and instead the sheet under the punch is subjected to tensile load. The present simulation was able to capture this interesting effect. This builds an interesting implication on possible rupture of foil and separator under the punch.

8.5 Confined Compression Test of the Prismatic / Pouch Cell

In the third part of simulations, the confined compression in the width direction was modeled. To model the buckling of layers as observed in the experimental test, it was required to represent the metal foil layers in a more realistic way. Therefore, metal foils were modeled with adding shell elements on the top and bottom surfaces of each layer of solid element. Considering solid elements of 0.24mm in depth, it yields that each solid element represents one layer of the multi-material system which includes two foils. This model was used to show a qualitative representation of the buckling phenomena. However, as the number of foils is half of its real value, their cross sections are 0.03mm to represent a similar order of moment of inertia. A more detailed model of layers will be built in the future to capture properties of the cell more realistically in this direction. Figure 45 below shows the formation of buckling waves in the layers of foil through the cross section. It can be observed that first waves were formed at the center of cross section and then consequent wave formation continued throughout the height of the cell. This type of wave formation indicates that foils underwent Euler type of buckling but due to confinement and the foundation of active powder material represented by solid elements, buckling mode is of a higher order rather than a single half-wave bending. Figure 46 below shows the load-displacement curve from simulation compared to the test. The curve was moved 0.6mm forward, because the model had no imperfection, and onset of buckling was before progress of any displacement, while it is not the case in real tests.

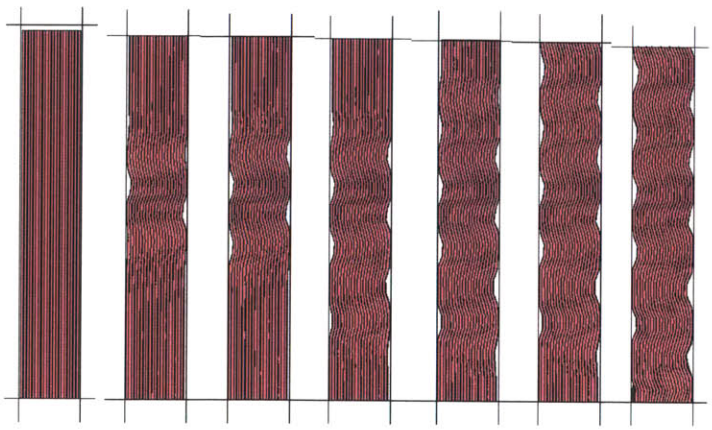

Figure 45 Confined Compression of the Cell in Width Direction Showing Development of Multiple Buckles

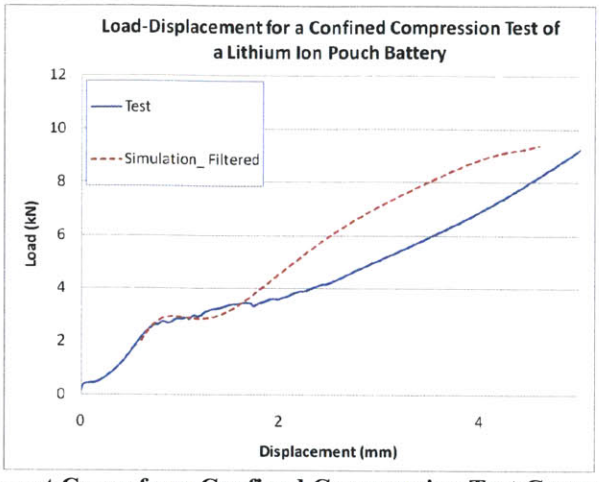

Figure 46 Load Displacement Curve from Confined Compression Test Compared with the Simulation

The current model for the confined compression included 30,000 solid and 31,500 shell elements. Using 6 CPU's to run the simulation, it took 22 hours to run. For a more representative model, it would be ideal to model all 42 layers of foil with their actual thickness. However, doing so would have required reducing the thickness of solid elements to 0.12mm, and consequently would decrease the time step size. The time step could be controlled using mass scaling methods, as the current simulation is quasi-static, but the model would not be useful for dynamic simulations in future. Another issue is that decreasing length of element in thickness direction to 0.12mm would require decreasing the element size in length and width direction as well. It is recommended that the aspect ratio of elements remain under 5/1 which means the maximum element size in width and length direction would also decrease to 0.6mm or smaller. This would cause an increase of about 8 times in the number of solid elements, and therefore, it would cause another significant increase in total CPU usage and simulation time. Therefore, a more refined mesh was not used for purpose of the current study.

9. Application to the Crush Loading of Battery Modules with a Metal Housing

There has been a debate within the battery industry about the merits of using the cylindrical or prismatic batteries in vehicles (32). It transpires from the results of the present study that the structural integrity of the cylindrical battery is consistent and high in all loading directions. At the same time prismatic/pouch batteries are strong when compressed in the thickness direction and weak in other directions. The average mechanical properties of the RVE in the cylindrical cells is the same in all three directions leading to a relatively small quasi-isotropic material model. The comparison of the stress-strain curve of the cylindrical cell with that of the active material with binder in the prismatic cells is shown below in Figure 47. The shape of the two curves is entirely different. A full understanding of the above distinct behavior would entail a detailed analysis of buckling, delamination, and friction between the subsequent layers.

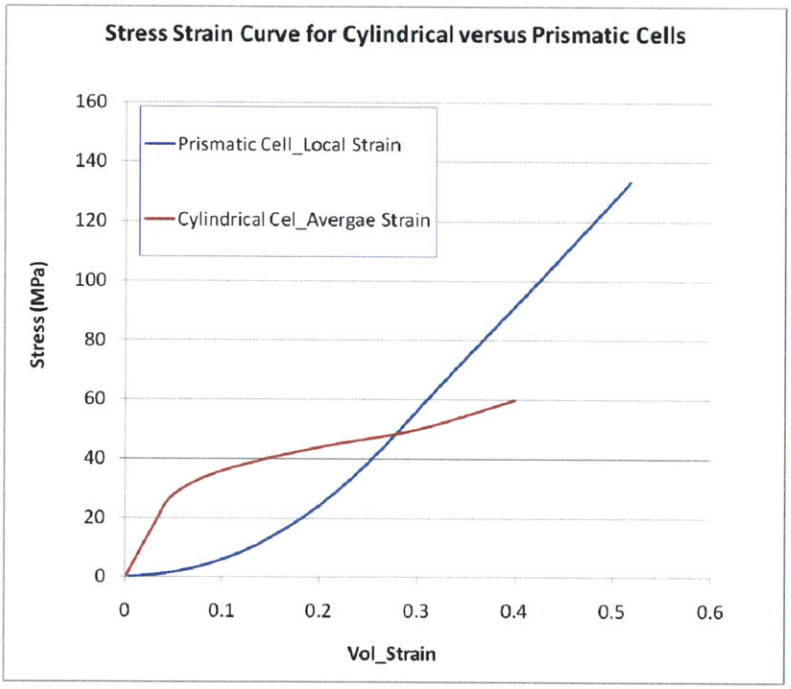

Figure 47 Comparison of the Average Stress-Volumetric Strain of the Cylindrical Battery and the Local Stress-Strain Curve of the Rectilinear Battery Compressed in the Thickness Direction

Portions of the above differences come from different definitions of compression-strain used in converting measured load-displacement relation to the stress-strain curves. In the case of the above prismatic cells the strains are local strains averaged over the thickness of the electrode / separator assembly. For the cylindrical cell, the strain is defined through the average diameter of the cell. In other words, mechanical properties of both types of batteries should be compared using a similar measure of strain.

The present paper has identified the importance of the amount of lateral battery constraints on its strength. Only two limiting cases were considered; one with unconfined compression and the other with full confinement. For the development of constitutive models and to better understand the local deformation mechanisms, a test program should be designed with a controlled amount of pre-compression. A suitable device was constructed in the Impact and Crashworthiness Lab at MIT, Figure 48.

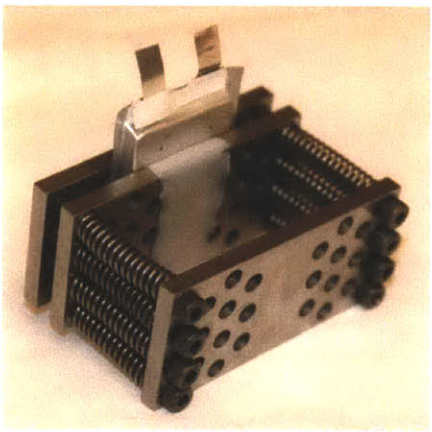

Figure 48 Prototype of the Plane-Strain Compression of Pouched Batteries with an Adjustable Confinement

10. Conclusions and Recommendations

From the present experimental and computational study the following conclusions may be drawn:

(i) Pouched and bare batteries exhibited different failure modes and produce different force levels. In the case of the present batteries, the shell casings were made of thin, approximately 0.1mm Mylar foil. It was interesting to see that such an apparently-thin membrane with very low bending stiffness could exert significant confinement to the cell and thus change its properties. This observation indicates the importance of a properly-designed shell casing for any type of prismatic battery. For the wound cylindrical batteries, each subsequent layer provides confinement to interior layers, therefore, the thickness of the shell casing may not be that important but this problem was not addressed.

(ii) The test and simulation proved that the layered structure of flat prismatic batteries is extremely anisotropic where the strengths in the thickness direction are much larger than the strengths in the in-plane direction.

(iii) The theoretical analysis and numerical simulation of the confined compression prove that there is an intrinsic scaled parameter characterizing the lengths of the internal buckling waves. The challenge is to include this parameter in a complete constitutive model of the battery interior.

(iv) Another parameter controlling the mechanical properties of batteries is the amount of confining pressure which, in the language of mechanics, is usually measured by either hydrostatic stress or normal stress. It would therefore appear that a first order constitutive model of the battery interior could be constructed as an anisotropic Coulomb-Mohr type of material.

The ongoing research for the Battery Consortium at the Impact and Crashworthiness Lab at MIT will soon provide new practical solutions. In particular, an outstanding question of merits of cylindrical vs. prismatic batteries could be resolved using the presented methodology, (29).

The new battery consortium launched by the Impact and Crashworthiness Lab at MIT will continue examining this contribution by the individual constituents of the electrode separator assembly (20). Eventually this research will allow a prediction of the onset of an electric short circuit, preventing thermal runaway.

Figure 49 Toyota Prius Hymotion battery pack and an example of a battery module to be tested at the MIT dual actuator loading frame

References

1. *Evaluation of crash protection for Hybrid Electrical Vehicle under rear impact.* **Lim J. M., Seo S., Suk J., Kim G.** 2008, SAE World Congress No. 2008-01-0189.

2. *Investigation for Flame-retardant additives for safety usage of lithium ion batteries.* **Otsuki M., Ogino T., Amine Kh.** 2006, ESC Transactions, pp. 13-19.

3. *Safety Performance for phosphate based large format lithium-ion battery.* **Nguyen J., Taylor Ch.** 2004, INTELEC, pp. 146-148.

4. *Design and development for production of the Think EV battery pack.* **Ashtiani, C.** 2009. AABC-09 Conference.

5. *Intercalation-Induced stress and heat generation within single Lithium-ion battery cathode particles.* **Zhang X., Sastry A.M., Shyy W.** 2008, Journal of the Electrochemical Society, pp. 155 (7) A542-A552.

6. *Packing, intercalation, and compression: determination of operating stresses in composite Li Cathodes.* **Chen, Y.H., Wang, C.W., Zhang X., Shyy, E., Sastry, A.M.** 2006. ESC 210 meeting.

7. *Numerical modeling of electrochemical-mechanical interactions in Lithium polymer batteries.* **Golmon, S., Maute, K., Dunn, M.** 2009, Computers and Structures, pp. 87 1567-1579.

8. *Issues and Challenges Facing Rechargeable Lithium Batteries.* **Tarascon, J. M. and Armand, M.** 359-367, s.l. : Nature International Weekly Journal of Science, 2001, Vol. 15 November.

9. Battery Space. [Online] [Cited: Dec 1, 2010.] http://www.batteryspace.com/li-ionsinglecell.aspx.

10. *Building a Better Battery.* **Chiang, Y-M.** 6010, s.l. : Science, 2010, Vol. 330.

11. **Cavas, Christopher P.** SEAL Mini-sub Won't Be Repaired. *DefenseNews.* 2009, July 27.

12. *Homogenized constitutive model of the cylindrical lithium-ion battery cell.* **Sahraei E., Hil R., and Wierzbicki T.** 2010, Journal of Power Resources.

13. *Axial compression of foam-filled thin-walled circular tubes.* **Reddy, T. Y. and Wall, R. J.** 2, s.l. : International Journal of Impact Engineering, 1988, Vol. 7. 151-166.

14. *Experimental and numerical studies of foam-filled sections.* **Santosa S., Wierzbicki T., Hanssen A., Langseth M.** 2000, International Journal of Impact Engineering, pp. (24) 509-534.

15. *Static crushing of square aluminum extrusions with aluminum foam filler.* **Hanssen A.G, Langseth M., Hopperstad OS.** 1999, International Journal of Mechanical Sciences, pp. 41(8), 967-993.

16. *On the modeling of crush behaviour of a closed-cell aluminum foam structure.* **Santosa S., Wierzbicki T.** 1998, Journal of the Mechanics and Physics of Solids, pp. 46 (4), 645-669.

17. *Bending collapse of thin-walled beams with ultralight filler: numerical simulation and weight optimization.* **Chen W., Wierzbicki T., Santosa S.** 2002, Acta Mechanical, pp. (153) 183-206.

18. *Dual-indentation technique for the assessment of strength properties of cohesive-frictional materials.* **Ganneau, F. P., Constantinides, G. and Ulm, F.-J.** 1727-1745, s.l. : International Journal of Solids and Structures, 2006, Vol. 43.

19. *Effects of Concentration-Dependent Elastic Modulus on Diffusion-Induced Stresses for Battery Applications.* **Deshpande, R., Qi, Y. and Cheng, Y.-T.** A967-A971, s.l. : Journal of Electrochemical Society, 2010, Vol. 157.

20. **Baker, W. E., Togami, T. C. and Weydert, J. C.** Static and Dynamic Properties of High-Density Metal Honeycombs. *International Journal of Impact Engineering.* 1998. Vols. 21(3), 149-165.

21. **Timoshenko, S.** *Theory of Elastic Stability.* 1936 : McGraw-Hill.

22. *Modeling of lithium ion batteries for thermo-mechanical integrity.* **Wierzibicki, T., Anand, L. and Mohr, D.** Cambridge, MA : MIT, 2011-2013.

23. *Indentation of tubes under combined loading.* **Wierzbicki T, Suh MS.** 1988, International Journal of Mechanical Sciences, pp. Vol. 30, No ¾, pp. 229-248.

24. *Impact damage of long plastic cylinders.* **Hoo Fatt, M. and Wierzbicki, T.** United Kingdom : s.n., 11-16 August 1991. International offshore and polar engineering conference.

25. *Damage of ring stiffened cylenders under dynamic pressure loading.* **Hoo Fatt, M. and Wierzbicki, T.** San Fransisco, USA : s.n., 14-19 June 1992. International offshore and polar engineering conference.

26. *Damage of plastic cylinders under localized pressure loading.* **Hoo Fatt, M. and Wierzbicki, T.** 1991, International Journal of Mechanical Sciences, pp. Vol.33, No 12, pp 999-1016.

27. *Denting analysis of ring stiffened cylindrical shells.* **Hoo Fatt, M. and Wierzbicki, T.** 1991, International Journal of offshore and polar engineering, pp. June Vol 1., No. 2.

28. *crushing of tubes between rigid plates.* **De Runtz, J. A. and Hodge, P. G.** 1963, Applied Mechanics, pp. Vol. 30, 381-395.

29. *Design and Fabrication of Multifunctional Structural Batteries.* **Liu, P., Sherman, E. and Jacobsen, A.** 646-650, s.l. : Journal of Power Sources, 2009, Vol. 189.

30. *Li-Ion Cells with Experimental Validation.* **Wierzbicki, T., Sahraei, E. and Hill, R.** s.l. : Journal of Power Sources, 2011.

31. *Macroporous poly(vinylidene fluoride) membrane as a separator for lithium-ion batteries with high charge rate capacity.* **Dijan, D., et al.** 575-580, s.l. : Journal of Power Sources, 2009, Vol. 187.

32. **Berchevskiy.** private communication. 2010.

33. *Axial compression of foam-filled thin-walled circular tubes.* **Wall, T. Y. Reddy and R. J.** 1988, International Journal of Impcat Engineering, pp. Volume 7, Issue 2, Pages 151-166.

34. **Wierzbicki T., Mohr D.** Cambridge, MA : MIT, January 2011- December 2013. Industrial fracture consortium.

35. *From our readers: On the electronic conductivity of phospho-olivines as lithium storage electrodes.* **Ravet, Nathalie, Abouimrane, Ali and Armand, Michel.** 2, 702, 2003.

36. **Polmar, Norman.** Military.com. *Problems Persist for SEAL Mini-Subs.* [Online] December 16, 2008.